JACS
JOURNAL OF THE AMERICAN CHEMICAL SOCIETY
pubs.acs.org/JACS
Article

Spatiotemporal Heterogeneity of Temperature and Catalytic Activation within Individual Catalyst Particles

Yu Tian,[§] Mingbin Gao,*[,§] Hua Xie, Shuliang Xu, Mao Ye,* and Zhongmin Liu

Cite This: J. Am. Chem. Soc. 2024, 146, 4958−4972
Read Online

ABSTRACT: Temperature is a critical parameter in chemical conversion, significantly affecting the reaction kinetics and thermodynamics. Measuring temperature inside catalyst particles of industrial interest (~micrometers to millimeters), which is crucial for understanding the evolution of chemical dynamics at catalytic active sites during reaction and advancing catalyst designs, however, remains a big challenge. Here, we propose an approach combining two-photon confocal microscopy and state-of-the-art upconversion luminescence (UL) imaging to measure the spatiotemporal-resolved temperature within individual catalyst particles in the industrially significant methanol-to-hydrocarbons reaction. Specifically, catalyst particles containing zeolites and functional nanothermometers were fabricated using microfluidic chips. Our experimental results directly demonstrate that the zeolite density and particle size can alter the temperature distribution within a single catalyst particle. Importantly, the observed temperature heterogeneity plays a decisive role in the activation of the reaction intermediate and the utilization of active sites. We expect that this work opens a venue for unveiling the reaction mechanism and kinetics within industrial catalyst particles by considering temperature heterogeneity.

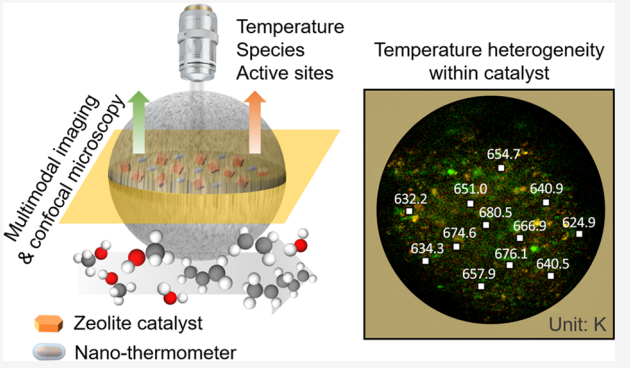

INTRODUCTION

Heterogenous catalysis by porous solid catalysts such as zeolites is of great importance in the efficient and sustainable conversion of carbon-based resources (e.g., crude oil, coal, biomass, natural gas, and CO_2) for producing valuable chemicals.[1−4] The essence of catalyst development lies in the optimized active sites[5,6] and anticipated reaction rates,[7] enabling on-purpose chemical reactions to proceed with high efficiency, mild conditions, and low cost. Temperature, a direct indicator of the kinetic energy and collisional frequency of reacting molecules, determines the kinetics and thermodynamics of chemical reactions.[7,8] In real applications, measuring the reactor temperature has become a common practice to monitor the apparent reaction performance of bulk catalysts including but not limited to the reaction rate, heat and mass transfer, reactant conversion, and product yields.[9,10] In practical chemical industries, catalytic active sites are commonly sealed in grain to reduce the mass transfer resistance or make catalyst particles readily fluidized.[11−13] Despite its significance, temperature as the most decisive operating parameter in catalysis, however, has yet to be carefully studied at the single catalyst particle. In particular, lacking real-time temperature information at local active sites inside catalyst particles greatly hinders the insightful understanding of the reaction mechanism in heterogeneous catalysis. Therefore, measuring temperature at catalytic sites within catalyst particles remains a nontrivial task.[14,15]

At the single catalyst level, temperature has proved to be closely related to the structure of active sites (e.g., sintering of metal clusters[16] and vibration of protonic acid[17,18]), the reactivity of the intermediate,[19,20] and the intrinsic reaction rate and molecular diffusion.[21] Recently, Weckhuysen and his co-workers found that the temperature difference between the local external catalyst surface and the reactor bed can be up to +16 K for methane oxychlorination[22] and +40 K for syngas to hydrocarbons.[8] However, for solid porous catalysts, the active sites are usually decorated as catalytic substrates within the catalyst particles.[12,23] This suggests that the local temperature at active sites inside a single catalyst could deviate significantly from the expected reactor temperature. Meanwhile, with the advance of the exploitation of spatiotemporal-resolved spectroscopy, anisotropic reaction rates have been commonly observed within individual catalyst particles. Using a confocal fluorescence microscope[13] (CFM) or an infrared microscope[24] (IRM), the spatial heterogeneous distributions of Brønsted acid sites (BAS) and carbonaceous intermediates within a

Received: December 18, 2023
Revised: January 24, 2024
Accepted: January 26, 2024
Published: February 9, 2024

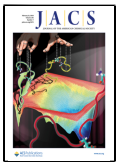

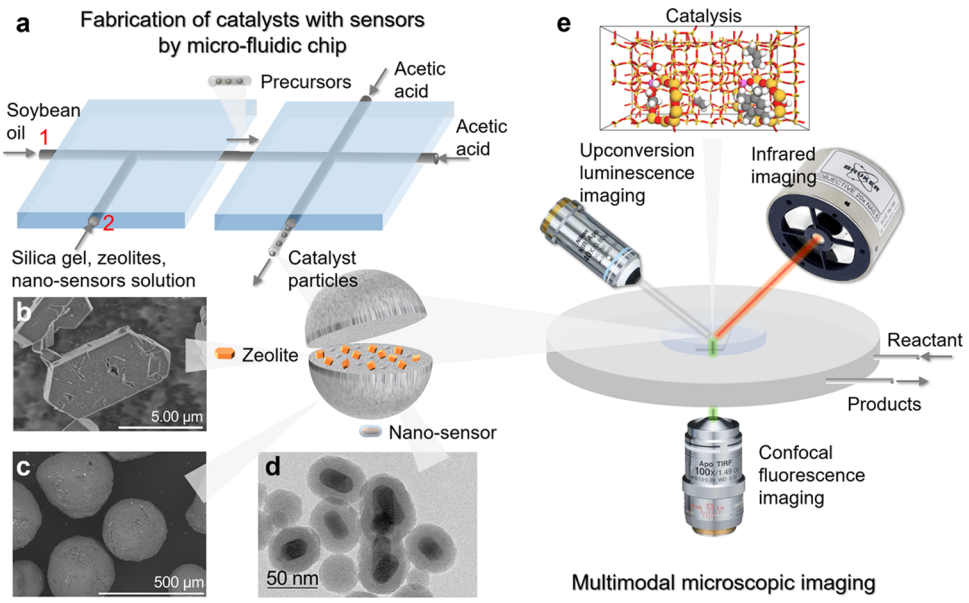

Figure 1. Schematic illustration for fabrication of catalyst particles and multimodal imaging techniques. (a) Schematic diagram of fabrication of catalyst particles containing zeolites, a nanothermometer, and a SiO_2 binder by T-shaped combined with cross-shaped microfluidic chips. Typical morphology of the prepared catalyst particles: scanning electron microscopy images of (b) H-ZSM-5 zeolites and (c) catalyst particles, and (d) transmission electron microscopy images of $NaYF_4$@SiO_2 nanoparticles. (e) Schematic diagram of multimodal imaging, i.e., upconversion luminescence imaging, infrared microscopy, and super-resolution confocal fluorescence microscopy to monitor spatiotemporal evolutions in temperature, active sites, and carbonaceous species within individual catalyst particles during the methanol-to-hydrocarbons reaction.

single zeolite crystal or catalyst particles in different reaction stages of hydrocarbon conversions have been demonstrated. In addition, heterogeneous concentration profiles of guest molecules within zeolites or catalyst particles during the uptake process, which are directly relevant to molecular diffusion, have also been depicted by IRM,[25] CFM,[11] and interference microscope.[26] The spatial heterogeneity of active sites and guest molecules within a single catalyst will undoubtedly lead to the spatial distribution of the reaction rate. Consequently, the quantity of heat (estimated by the product of the reaction rate and enthalpy) and temperature change aroused by reactions may vary in both space and time inside a single catalyst particle. Therefore, directly measuring the temperature distribution inside individual catalyst particles and further understanding the effects of local temperature on reaction dynamics at active sites (e.g., guest molecular activation, intermediates formation, and active site utilization) remain considerable challenges in heterogeneous catalysis.

Electricity-based (e.g., invasive multiple thermocouples[9]) and spectroscopy-based (e.g., nonintrusive infrared,[27] nuclear magnetic resonance,[28] and Raman[29]) thermometries are often applied to detect spatiotemporal evolution of temperature and evaluate the thermal effect in the catalyst bed of the reactor. However, the spatial resolutions of these thermometric techniques are limited to millimeters, restricting their applications for individual catalyst particles with sizes of industrial interest (~microns). Luminescence thermometries,[8,30−35] which rely on the changes in adsorption or emission spectrum induced by temperature variations, provide a potential way for nonintrusive local temperature sensing with sufficient spatial and temporal resolution. For instance, the luminescence of lanthanide ions Er^{3+}, Nd^{3+}, or Eu^{3+} in inorganic hosts excited by near-infrared light (980 or 785 nm) or UV light is temperature-dependent. Implementing the upconversion spectrometer to detect the luminescence spectra of Yb^{3+},Er^{3+}-codoped $NaYF_4$@SiO_2 nanoparticles[36] adhered to the catalyst surface or mixed with the catalyst can obtain the local surface temperature of the individual catalyst or catalyst bed with transparent walls during hydrocarbon conversions.[37] Spatially resolved detection of the upconversion luminescence (UL) spectra of Y_2O_3 doped with Nd^{3+} mixed in Ni/TiO_2 catalysts can obtain the local temperature of the catalyst surface during CO_2 methanation.[35] In the methane oxychlorination reaction catalyzed by EuOCl, the fluorescence emission spectra of the catalyst material can also be used to operando determine the local surface temperature in the fixed-bed reactor.[22] As discussed, implementing lanthanide-doped temperature nanosensors stimulated notable advances in the local surface temperature measurement at individual catalyst levels. However, the technologies based on either the luminescence or fluorescence emission spectra require the measuring points to be optically accessible, which constrains that only local temperature at the catalyst surface can be detected.[8,22] Thus, these developed techniques cannot be used to study the interplay between local temperature distribution and heterogeneous catalytic activity inside a single catalyst particle.

Here, we propose to use two-photon confocal microscopy with state-of-the-art upconversion luminescence (UL) imaging to measure spatiotemporal-resolved temperature distribution within individual H-ZSM-5 zeolite catalyst particles in the industrially significant methanol-to-hydrocarbons (MTH) reaction. Methanol can be readily converted into valuable hydrocarbons over zeolite catalysts, which are attractive building blocks for sustainable fuels and chemicals.[38,39] In addition, the MTH reaction is an archetypal strong exothermic reaction with hydrocarbon pool (HCP) as the controlling mechanism,[38,40−42] which thus is selected as a model reaction in this work. The product selectivity[43,44] and catalyst lifetime[45] in MTH depend upon the activation of HCP species, which

https://doi.org/10.1021/jacs.3c14305
J. Am. Chem. Soc. 2024, 146, 4958−4972

are highly sensitive to temperature.[38,46] Direct observation of the effects of temperature heterogeneity on the efficiency of active sites and activation of HCP species within individual catalyst particles can profoundly unveil the reaction mechanism and kinetics under actual operating conditions. To this end, we first applied microfluidic chips to fabricate catalyst particles containing H-ZSM-5 zeolites and functional nanosensors (luminescence nanothermometry Yb^{3+},Er^{3+}-codoped $NaYF_4$@SiO_2 in this work) to imitate industrial catalysts (Figure 1a). Then, using confocal two-photon microscopy, we can measure the temperature distribution inside individual catalyst particles based on the ratiometric thermometry of nanothermometry embedded in a catalyst. Thus, a multimodal imaging approach,[47] which combines a super-resolution confocal fluorescence microscope[48] (CFM), IRM,[24,49] and UL imaging, was utilized to monitor carbonaceous species formation and BAS utilization, together with temperature distribution inside individual catalyst particles (Figure 1e). Based on the multimodal images of well-prepared catalyst samples (catalysts with similar particle sizes but different zeolite densities and catalysts with similar content of zeolites but different particle sizes), the heat transfer process and the effect of heat release and thermal conductivity aroused by an exothermic MTH reaction on the utilization of active sites and activation of HCP species can be well elucidated. It is discovered that at a low start-up temperature, large heat discharge and a lower temperature gradient within a single catalyst particle favor fully activating hydrocarbon pool species and thus enlarging the throughput of the reactant in bulk catalysts. We show that spatiotemporal heterogeneity of temperature within individual catalyst particles has a crucial impact on catalyst performance, which should be considered to be an indispensable factor in the rational design of solid porous catalysts.

RESULTS AND DISCUSSION

Fabrication of Catalyst Particles Containing Functional Nanosensors. For catalyst particle fabrication, T-shaped and cross-shaped microfluidic chips[50,51] were employed, as shown in Figure 1a. In T-shaped microfluidic chips, soybean oil was injected as an oil-continuous phase into entrance 1. Silica gel (as a source of binder), Na-ZSM-5 zeolites (Si/Al is 36.2, and for the characterization, see Figure S3), and Yb^{3+},Er^{3+}-codoped $NaYF_4$@SiO_2 nanoparticles ($NaYF_4$@SiO_2 for short; for the characterization, see Figure S1) were premixed and injected as a water-continuous phase into entrance 2. Regulating the ratio of zeolites to silica gel can control the content of zeolites in catalyst particles, while $NaYF_4$@SiO_2 was fixed at 8 wt %. In addition, controlling the flow rate of the water phase can regulate the size of the catalyst particles. At the intersection of the oil and water phases, under the surface tension of the water phase in the oil phase, aqueous droplets, i.e., precursors of catalyst particles, were formed and injected into a cross-shaped microfluidic chip. In the cross-shaped microfluidic chip, adjusting the pH value of the solution to neutrality by acetic acid can facilitate the solidification of precursors to catalyst particles. Subsequently, catalyst particles containing H-ZSM-5 were obtained by a successive ion exchange method. According to the above experimental procedures, customized catalyst particles were obtained (for the characterization, see Figure S4 and Tables S1 and S2). One is catalyst particles with a similar particle size (330 μm; the particle sizes of catalyst samples were counted by a scanning electron microscope) but contained different contents of zeolites (15, 25, and 35 wt % of zeolites, which are named CAT-15% zeo., CAT-25% zeo., and CAT-35% zeo., respectively) to achieve different heat conductivities between samples. The other one is catalyst particles with similar content of zeolites (25 wt %) but with different particle sizes (270, 300, and 330 μm of particle sizes, which are named CAT-25% zeo. (S), CAT-25% zeo.(M), and CAT-25% zeo., respectively) to achieve different temperature gradients between samples. These particle sizes of the catalyst are designed to imitate the industrial catalyst used in the MTH process.[52] It needs to be emphasized that the nanosensors embedded into the catalyst are not limited to nanothermometers. Nanoparticles can be versatile functional nanosensors, e.g., Au@SiO_2, to detect surface−hydrocarbon intermedia by confocal Raman spectroscopy[8,53] and to satisfy the needs of spatiotemporal-resolved characterization of local conditions, chemical species, and surface intermedia within the individual catalyst.

The structure and crystalline of pristine and calcined $NaYF_4$@SiO_2 (at 773 K) were examined by high-resolution transmission electron microscopy and X-ray powder diffraction (Figure S1), respectively, which show the excellent thermostability of $NaYF_4$@SiO_2. In this work, the major function of the coating of the SiO_2 nanoshell deposited on $NaYF_4$ is to prevent the degradation of the crystal structure of $NaYF_4$ following the research[8,31,37] by Weckhuysen and co-workers. The SiO_2 nanoshell will mainly influence the luminescence intensity of $NaYF_4$ excited by a 980 nm laser. Chen et al.[54] found that as the thickness of the SiO_2 nanoshell increased from 0 to 14 nm, the emission peak intensity of $NaErF_4$ gradually increased, which can be explained by the fact that the coating of the SiO_2 shell can reduce the surface defects of the luminous core particle. However, as the thickness of the SiO_2 nanoshell further increases from 14 to 30 nm, the emission intensity gradually decreases. This implies that a SiO_2 nanoshell on the luminous core particle that is too thick will block the radiation of 980 nm excitation light to Er^{3+} and is not conducive to upconversion luminescence. In this work, the thickness of the SiO_2 shell is ∼12 nm, as shown in Figure S1, which is close to the optimized thickness of the SiO_2 shell reported by Chen et al.[54] Geitenbeek et al.[31] compared the ratiometric-based thermometry between $NaYF_4$ and $NaYF_4$@SiO_2 coated with a 10 nm SiO_2 nanoshell using the intensity ratio between $^2H_{11/2}$ and $^4S_{3/2}$. They found that the energy difference between the excited states ΔE of $NaYF_4$@SiO_2 (716 cm^{-1}) is similar to that of $NaYF_4$ (714 cm^{-1}), which can illustrate that coating the 10 nm SiO_2 nanoshell on $NaYF_4$ has a slight influence on the temperature measurement accuracy of the $NaYF_4$ core particle. In this work, the thickness of the SiO_2 nanoshell on $NaYF_4$ is ∼12 nm following the recipe from Geitenbeek et al.,[31] which indicates that the effect of the SiO_2 nanoshell on $NaYF_4$ in this work on temperature measurement accuracy can be neglected. The content of H-ZSM-5 in catalyst particles was verified by quantitative BAS amount measurement, as shown in Table S2. The reactive probe-molecule furfuryl alcohol (FA), which can be converted into fluorescent products over BAS,[55] was specifically selected to stain the H-ZSM-5 zeolites. Figure S6 shows the uniform distribution of H-ZSM-5 within all catalyst samples.

Spatiotemporal-Resolved Measurements of Temperature within Individual Catalyst Particles. The simplest way for luminescence thermometry is based on the recording of absolute luminescence intensity (i.e., "single intensity"

https://doi.org/10.1021/jacs.3c14305
J. Am. Chem. Soc. 2024, 146, 4958−4972

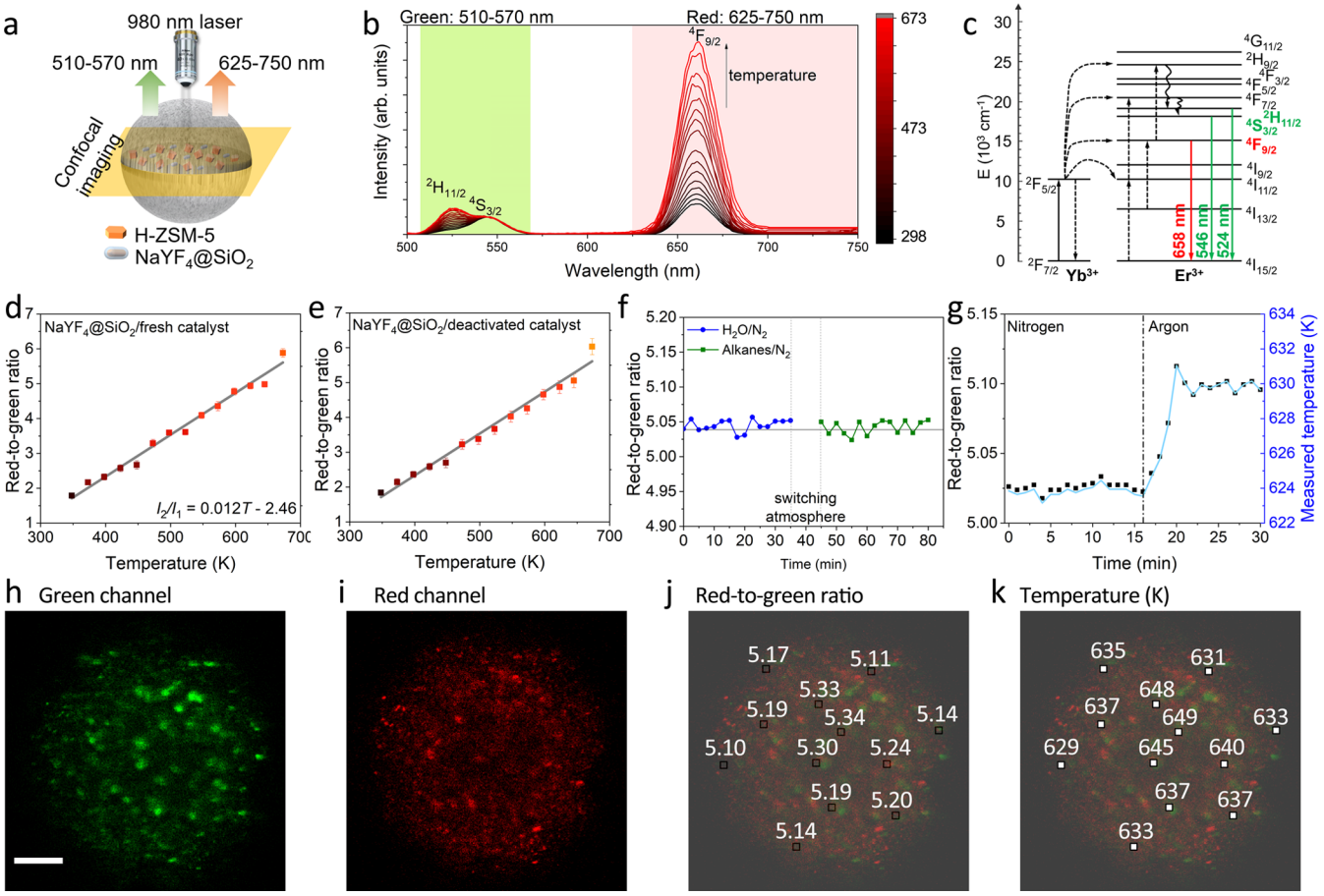

Figure 2. Illustration of nanothermometers for spatiotemporal measurements of temperature within individual catalyst particles. (a) Schematic detection of the luminescence intensity of $NaYF_4@SiO_2$ embedded within the catalyst at 510−570 (green channel) and 625−750 nm (red channel) excited by 980 nm lasers with the implementation of upconversion luminescence confocal microscopy. (b) Emission spectra of $NaYF_4@SiO_2$ in the CAT-25% zeo. catalyst upon excitation at 980 nm for temperatures ranging from 298 to 673 K recorded with steps of 25 K in nitrogen. (c) Energy level diagrams of $NaYF_4$:Yb^{3+},Er^{3+}. Solid, dotted, and wavy arrows represent photon absorption or emission, energy transfer, and relaxation processes, respectively. The linear relation between the integrated intensity ratio of the 625−750 and 510−570 nm bands of $NaYF_4@SiO_2$ in (d) fresh and (e) deactivated catalyst versus temperature in nitrogen. (f) The effect of the chemical atmosphere (steam and alkanes) on the red-to-green ratio of $NaYF_4@SiO_2$ in the catalyst at 623 K. The steam (0.03 bar) was carried by nitrogen at room temperature with a flow of 5 mL·min^{-1}. The main component of alkanes is propane, and the flow rate of alkanes is 5 mL·min^{-1}. (g) The red-to-green ratio (left axis) and temperature variation (right axis) of individual catalyst particles under a N_2 atmosphere to an Ar atmosphere at the initial temperature of 623 K. The gas flow is 5 mL·min^{-1}. Typical spatial-resolved luminescence intensity of $NaYF_4@SiO_2$ in the CAT-25% zeo. catalyst at (h) 510−570 nm, and (i) 625−750 nm at 623 K during MTH reactions. The scale bar is 50 μm. (j) The calculated red-to-green ratio based on (h) and (i). (k) The spatial distribution of temperature within the catalyst particle calculated by the red-to-green ratio in (j) combined with the calibration curve in (d). The pictures of (j) and (k) are, respectively, the overlay of (h) and (i), which are the schematic diagrams to indicate the position for red-to-green and temperature calculations (selected area: 3 × 3 μm^2).

method). This method, however, is vulnerable to the local concentration of the nanothermometers, the chemical environment (e.g., organic molecules), and the changes in material optical properties.[33] The methanol-to-hydrocarbons (MTH) process involves the dehydration and conversion of methanol to water, hydrocarbons, and coke over zeolites.[38,56] In addition, in Figure 2h,i, the concentration distribution of Yb^{3+},Er^{3+}-codoped $NaYF_4@SiO_2$ nanoparticles within the catalyst particle is nonuniform. In this work, we employ the ratiometric-based method, which could balance the quality, cost, and speed of detection and is considered so far to be the most promising approach.[8,31,33,34,37] It has been anticipated that the nonuniform concentration of $NaYF_4@SiO_2$ does not affect the thermal readout,[33] given that the excitation laser power remains the same.[57]

Figure 2b shows the UL emission spectrum of $NaYF_4@SiO_2$ embedded within the catalyst upon excitation at 980 nm. In the region between 500 and 750 nm, three distinct peaks are observed, centered around 524, 546, and 658 nm. These peaks correspond to the $^2H_{11/2}$−$^4I_{15/2}$, $^4S_{3/2}$−$^4I_{15/2}$, and $^4F_{9/2}$−$^4I_{15/2}$ transitions of Er^{3+}, respectively,[34] as shown in Figure 2c. As shown in Figure 2d, the red-to-green ratio is defined as the luminescence intensity ratio (LIR) I_2/I_1, where intensities of I_1 and I_2 are the integrated areas of the bands at, respectively, 510−570 and 625−750 nm shown in Figure 2b. By using confocal UL imaging, it can be found that the red-to-green ratio of $NaYF_4@SiO_2$ within the catalyst particle increases with increasing temperature in a linear relation. As shown in Figure 2e,f, we carried out experiments to verify that the color changes in catalysts by coking and chemical atmosphere (e.g., steam and alkanes) almost do not affect the temperature measure-

https://doi.org/10.1021/jacs.3c14305
J. Am. Chem. Soc. 2024, 146, 4958−4972

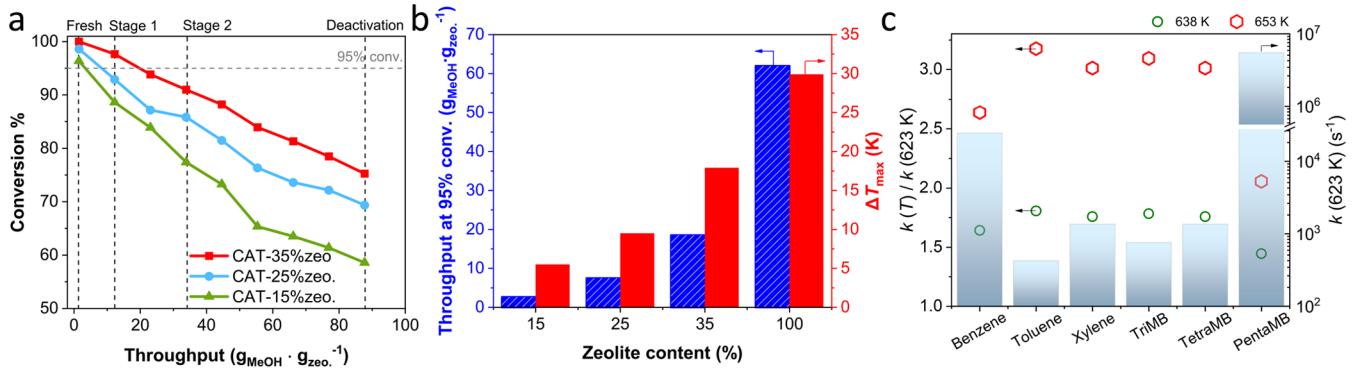

Figure 3. Effect of the zeolite density of catalyst particles on MTH reactions. (a) Methanol conversion as a function of methanol throughput over CAT.-35% zeo., CAT-25% zeo. and CAT-15% zeo. catalysts in a fixed-bed reactor. The initial reaction temperature is 623 K, and the weight hourly space velocity (WHSV) is 22.1 $g_{MeOH} \cdot g_{zeo.}^{-1} \cdot h^{-1}$ in the fixed-bed reactor (keeping the same amounts of zeolites in the catalyst bed). (b) Relation between methanol throughput (methanol conversion at 95% in (a), blue histogram)/maximum temperature rise (red histogram) and the content of H-ZSM-5 zeolites in the catalyst. Reaction conditions are the same as those shown in (a). (c) The ratio of reaction kinetic constants between 638 K (653 K) and 623 K (hollow point, green for 638 K and red for 653 K) and kinetic constants of polymethylbenzene methylation at 623 K (histogram). Free energy barriers $\Delta G^{\ddagger}$ were obtained from ref 60 of periodic density functional theory combined with the reorientation method developed by Hibbitts et al.[41,60,62] The reaction kinetic constant is estimated by $k = \frac{k_B T}{h} \exp(-\Delta G^{\ddagger}/RT)$

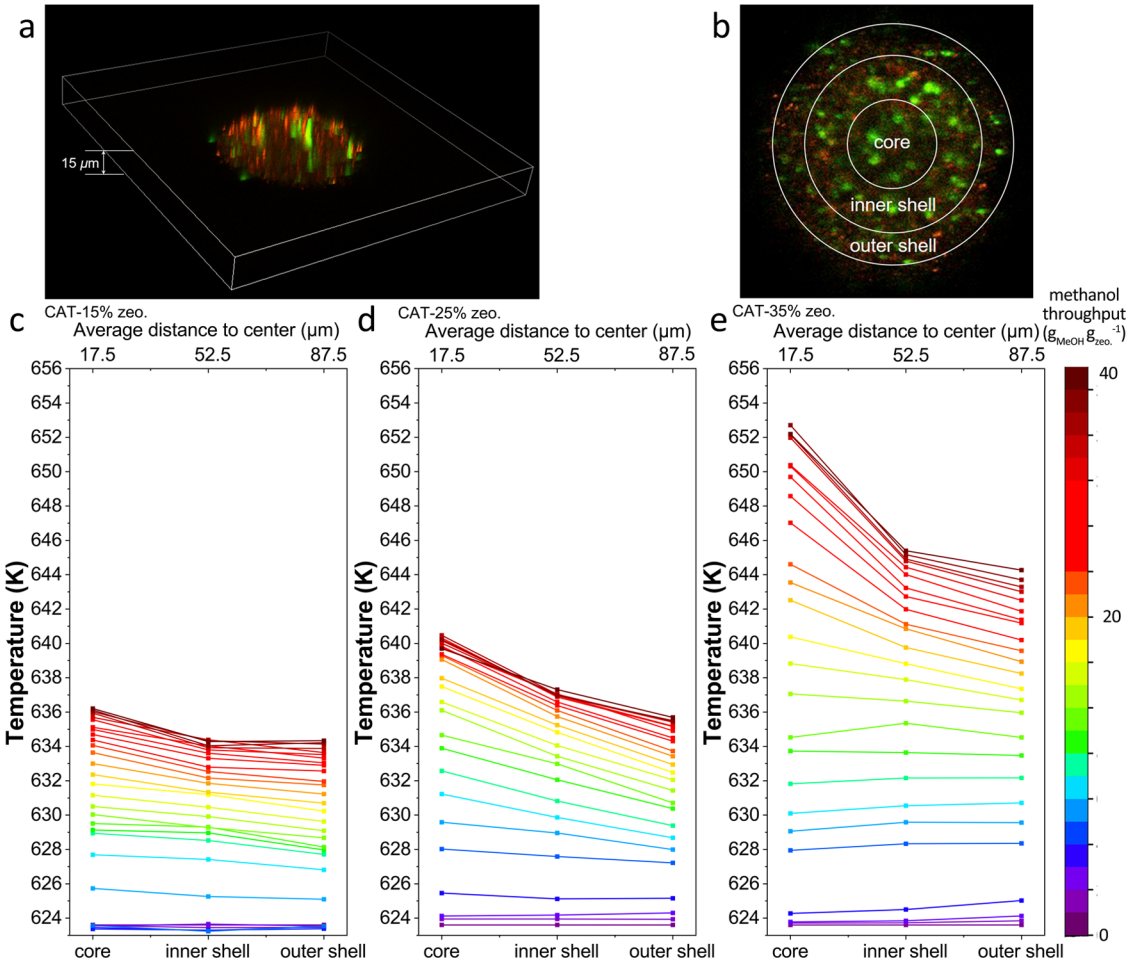

Figure 4. Spatiotemporal-resolved temperature measurements over catalyst particles with different zeolite densities during MTH reactions. (a) Three-dimensional reconstruction of the overlap luminescence intensity of $NaYF_4$@SiO_2 at 510−570 nm (green) and 625−750 nm (red) in the catalyst particle visualized by confocal UL microscopy at 623 K. (b) Focal plane for data analysis that is taken at the plane at z = 15 μm from the top in (a). The spherical cross section of the catalyst is divided into the core, inner-shell, and outer-shell regions for analysis. Spatiotemporal evolutions of temperature rise within individual (c) CAT-15% zeo., (d) CAT-25% zeo. and (e) CAT-35% zeo. catalyst particles by ratiometric thermometry using confocal UL microscopy during the MTH reactions. The initial reaction temperature is 623 K, catalyst loading in the reaction cell is 2 mg, and weight hourly space velocity is 22.1 $g_{MeOH} \cdot g_{zeo.}^{-1} \cdot h^{-1}$. The inlet of nitrogen to carry methanol saturated steam at room temperature is 2, 1.5, and 1 mL·min^{-1} for CAT.-35% zeo., CAT.-25% zeo. or CAT.-15% zeo. catalysts, respectively.

https://doi.org/10.1021/jacs.3c14305
J. Am. Chem. Soc. 2024, 146, 4958−4972

ments by ratiometric thermometry (see details in Supporting Note 6). As shown in Figure S7a,b, the absolute luminescence intensity at 510−570 and 625−700 nm emitted by $NaYF_4$@SiO_2 enclosed in the deactivated catalyst particles has been significantly reduced compared to that in the fresh ensemble catalyst particles, owing to the absorbance of coke within zeolites (Figure S8a). Meanwhile, we examined the ratio of the luminescence intensities of red and green lights emitted by $NaYF_4$@SiO_2 in both deactivated and fresh catalysts. As can be seen in Figure S7e,f, the calibration curve of temperature based on the LIR, i.e., red-to-green ratio, essentially remains the same for both deactivated and fresh catalyst particles. Though the absorbance or luminescence of coke species at 510−570 and 625−700 nm can be affected by many factors,[47] comparing the UL spectra of $NaYF_4$@SiO_2 in fresh and deactivated ensemble catalysts is the most effective way to examine the effect of coke formation on the red-to-green ratio of $NaYF_4$@SiO_2 in catalysts. This can be potentially evidenced by the similar absorbances of coke at 625−700 and 510−570 nm in the in situ diffuse reflectance (DR) UV−vis spectra in Figure S8b. Nevertheless, these measurements show that $NaYF_4$@SiO_2 can be used to monitor the temperature within the catalyst particle during MTH reactions based on the calibration curve shown in Figure 2d. The temperature measurements within catalysts by the red-to-green ratio were carried out under different carrier gases with distinct thermal conductivity, such as Ar and N_2 (respectively 31.5 and 45.3 $mW{\cdot}m^{-1}{\cdot}K^{-1}$ at 623 K).[58] As shown in Figure 2g, the red-to-green ratio of $NaYF_4$@SiO_2 in fresh CAT-25% zeo. was measured (∼5.02) in an in situ reaction cell at 623 K under nitrogen and recorded from 0 to 15 min. Subsequently, the nitrogen was switched to argon, and it can be observed that the red-to-green ratio of $NaYF_4$@SiO_2 in catalysts increases to 5.11, which corresponds to the temperature of 630.0 K estimated by the calibration curve in Figure 2d. Such results can strengthen the reliability of developed temperature measurement in this work.

Effect of Temperature on Activation of Hydrocarbon Pool Species. As shown in Figure 3c, the reaction kinetics of the methylation reaction (as the rate-determining step in aromatics-based cycles[59−61]) between aromatic species and methanol was used to estimate the activity of these species in H-ZSM-5 zeolite. Hibbitts et al.[41,60,62] developed a reorientation method to identify global minima and the most stable states of the reactant, product, and transition state with sufficient sampling based on the periodic density functional theory (DFT) calculations. The DFT calculations of polymethylbenzene methylation by Hibbitts et al.[60] are more quantitatively accurate. The intrinsic free energy barriers of polymethylbenzene methylation calculated by Hibbitts et al.[60,63] are used to obtain reaction kinetic constants for temperatures of 623, 638, and 653 K, as shown in Figure 3c. It can be found that increasing reaction temperature can be an effective means to enhance the activity of the polymethylbenzenes (polyMBs) with methanol, especially for the polyMBs with higher free energy barriers. Based on the Arrhenius equation, the degree of increase in a kinetic constant of intermedia with a high free energy barrier shows more sensitivity to the elevated temperature.[64] In this sense, polyMBs with higher free energy barriers of methylation, e.g., toluene, xylene, trimethylbenzene, and tetramethylbenzene, can be active intermedia. In contrast, these polyMBs show low activity at 623 K. Increasing temperature rise can prominently promote the activity and catalytic efficiency of aromatic species within the zeolite framework at low start-up reaction temperatures. Such distinct temperature-dependent activation of different polyMBs has been validated by transient $^{12}C/^{13}C$ methanol-switching experiments.[65,66]

Effect of Temperature Heterogeneity on Catalytic Efficiency within Individual Catalyst Particles. As shown in Figure 3b, in the bed of catalyst particles with the same BAS amounts but different BAS densities, it can be observed that a higher maximum temperature rise of the catalyst bed aroused by increased BAS density can enlarge the methanol throughput of the MTH reaction at a start-up temperature of 623 K. The UL imaging technique was implemented to unveil spatiotemporal temperature distribution within individual catalyst particles during the MTH reaction in an in situ cell under similar reaction conditions of the fixed bed. Figure 4a shows the three-dimensional (3D) reconstruction of $NaYF_4$@SiO_2 distributed in the catalyst particle by the emission excited by a 980 nm laser at 623 K. As shown in Figure 4b, the focal plane of the catalyst particle was selected as a plane at z = 15 μm from the top. Recently, Jacobs et al.[35] measured spatial temperature distribution on supported metal catalysts (Ni/TiO_2) with the addition of a luminescent thermometer Y_2O_3:Nd^{3+} by pixel-to-pixel mapping during CO_2 methanation. Under inert conditions, they found that the LIR of the luminescent thermometer vary spatially at a given temperature. They proposed three possible origins causing such spatially dependent LIR: spatial variations in absorption, scattering of thermometer emission by the sample, or background fluorescence. In this work, we also tried to measure spatially resolved temperature by pixel-to-pixel analysis of the red-to-green ratio within catalyst particles, as shown in Figures 2k and S10d. We found it difficult to directly calculate the red-to-green ratio at each pixel, especially by dividing of the whole picture into Figure 2h,i due to the heterogeneous distribution of $NaYF_4$@SiO_2 within particles. In addition, photon-counting noise will significantly affect the local red-to-green ratio when selecting too small a pixel size to analyze. As shown in Figure S10d, using a relatively large pixel size (3 μm × 3 μm) to measure the local red-to-green ratio and temperature, the relatively consistent temperature distribution within the catalyst is obtained under inert conditions. Therefore, to overcome the effect of these "errors" on spatiotemporal measurements of temperature, we select a relatively large area with sufficient statistics of the red-to-green ratio to measure temperature, as shown in Figure 4b. As shown in Figure 4b, the two-dimensional (2D) spherical plane is segmented into the core, inner-shell, and outer-shell regions as shown. The spatiotemporally heterogeneous evolutions of temperature within individual CAT-15% zeo., CAT-25% zeo. and CAT-35% zeo. catalyst particles (the plane at z = 15 μm) during the MTH reaction are shown in Figure 4c−e, respectively. We conducted 3D reaction−diffusion−heat transfer simulations (Supporting Note 6), which show that a similar temperature gradient in each cross section can be identified for catalyst particles at the same reaction time. Therefore, at the specific reaction time, based on the temperature of the external surface and temperature gradient of the plane at z = 15 μm, the temperature distribution can be extrapolated according to the radius of the interested cross section, as shown in Figure S13. At the initial stage, the temperature rise at the outer shell can be first observed, which is caused by the preferential reaction with methanol at the outer shell, as evidenced by the diffusion limitation of guests in

https://doi.org/10.1021/jacs.3c14305
J. Am. Chem. Soc. 2024, 146, 4958−4972

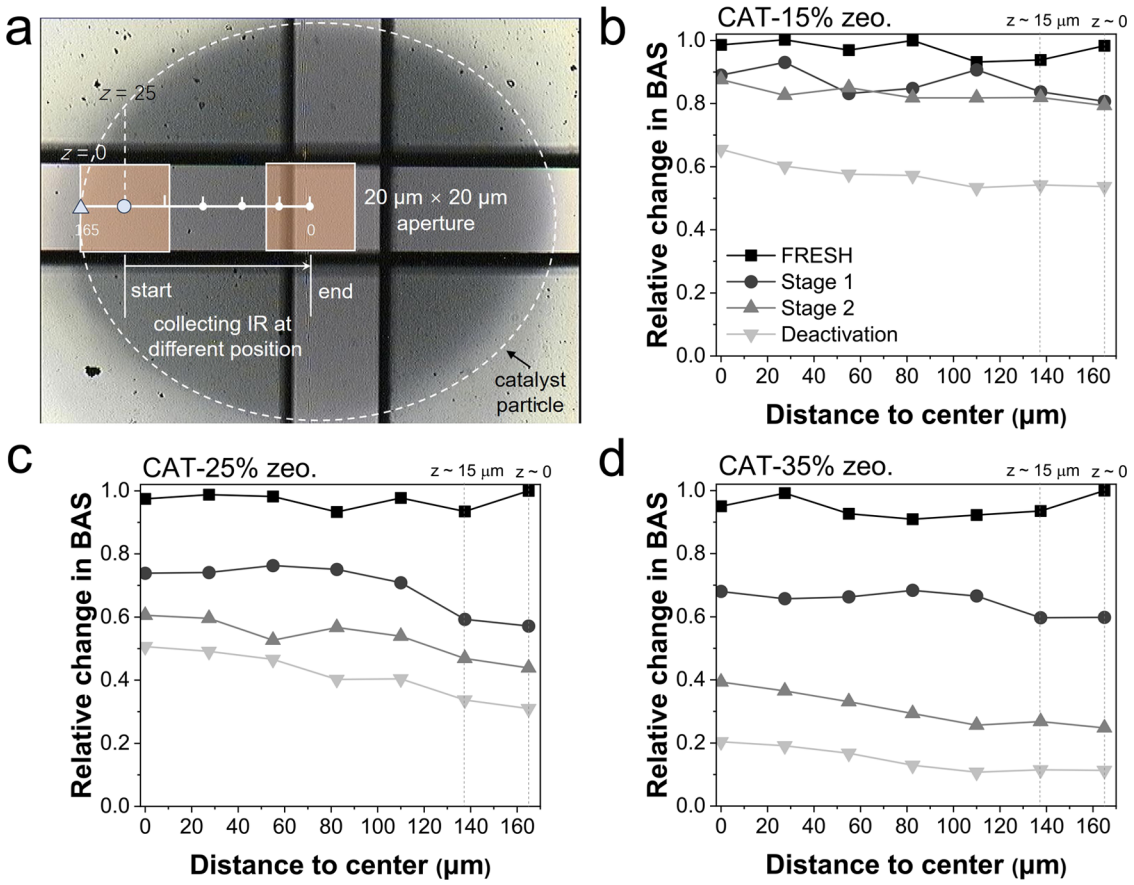

Figure 5. Spatiotemporal-resolved Brønsted acid sites within catalyst particles with different zeolite densities during MTH reactions. (a) Schematic measurements of infrared spectra at different locations of catalyst particles using IRM. The detection window of the infrared spectrum is 20 × 20 μm^2. Spatiotemporal evolutions of relative changes in BAS within individual (b) CAT-15% zeo., (c) CAT-25% zeo., and (d) CAT-35% zeo. catalyst particles by IRM at different MTH stages. Reaction conditions are the same as those shown in Figure 4c–e.

the catalyst shown in Figures S5 and S32. The reaction heat generated at the outer shell can rapidly conduct the inward core of the catalyst as the thermal conductivity κ of the binder (silica, ~600.0 $mW{\cdot}m^{-1}{\cdot}K^{-1}$) is significantly higher than that of the atmosphere (~45.3 $mW{\cdot}m^{-1}{\cdot}K^{-1}$ of nitrogen). Thus, the uniform distribution in temperature rise within a single catalyst at the initial MTH reaction can be observed. Subsequently, an adequate concentration of the reactant within the catalyst launches the MTH reaction in H-ZSM-5 zeolites located at the catalyst core region. However, the spherical shell area (i.e., heat-exchange surface) at the core region is inferior to that at the outer shell of the catalyst, which hampers the conduction of reaction heat and leads to a higher temperature rise at the core region. The higher temperature rise at the core region can further facilitate the activation or reaction rate of HCP species with methanol, as illustrated in Figure 3c, and release more reaction heat. Consequently, as the position gets closer to the catalyst center, the heating rate by the reaction exotherm is obviously faster. According to experiments, the heat conductivity coefficient of H-ZSM-5 zeolites (170.1 $mW{\cdot}m^{-1}{\cdot}K^{-1}$) is significantly lower than that of the SiO_2 matrix (600.0 $mW{\cdot}m^{-1}{\cdot}K^{-1}$). Combined with simulations shown in Figure S36, the high density of zeolites within the catalyst particle significantly reduces the heat conductivity coefficient of the catalyst particle. In the catalyst with more zeolites, the reaction heat generated at zeolites is inclined to further elevate local temperature rather than heat conduction. Meanwhile, the accelerated reaction rate promotes heat release to further elevate local temperature. Therefore, the integral temperature rise of the CAT-35% zeo. catalyst particle is higher than those of CAT-15% zeo. and CAT-25% zeo. samples. Hereto, the effect of zeolite density on temperature heterogeneity within individual catalyst particles can be well elucidated.

Advanced IRM and super-resolution CFM techniques further unveil the spatiotemporal evolutions of active sites[24] and carbonaceous species[11] formation resulting from above temperature heterogeneity in an in situ reaction cell. As shown in Figure 5b–d, the relative changes in the BAS of catalyst particles during different stages of the MTH reaction (Figure 3a) imaged by IRM are shown. For the pristine catalyst samples, the distribution of BAS within catalyst particles is uniform, which is consistent with the results of fluorescent molecule-staining experiments. During the MTH reaction, the BAS closed to the outer-shell region is preferentially covered by HCP species due to the high concentration of methanol at the catalyst rim (Figure S32). As shown in Figure 5d, the higher temperature rise caused by increased zeolite density within the catalyst leads to rapid coverage of BAS, while the formation and activation of HCP species are accelerated by elevated temperature. For the deactivated stage of the MTH reaction, it can be observed that the unexploited amounts of BAS in the CAT-35% zeo. sample is lower than those in CAT-15% zeo. and CAT-25% zeo. samples. This implies that the

https://doi.org/10.1021/jacs.3c14305
J. Am. Chem. Soc. 2024, 146, 4958–4972

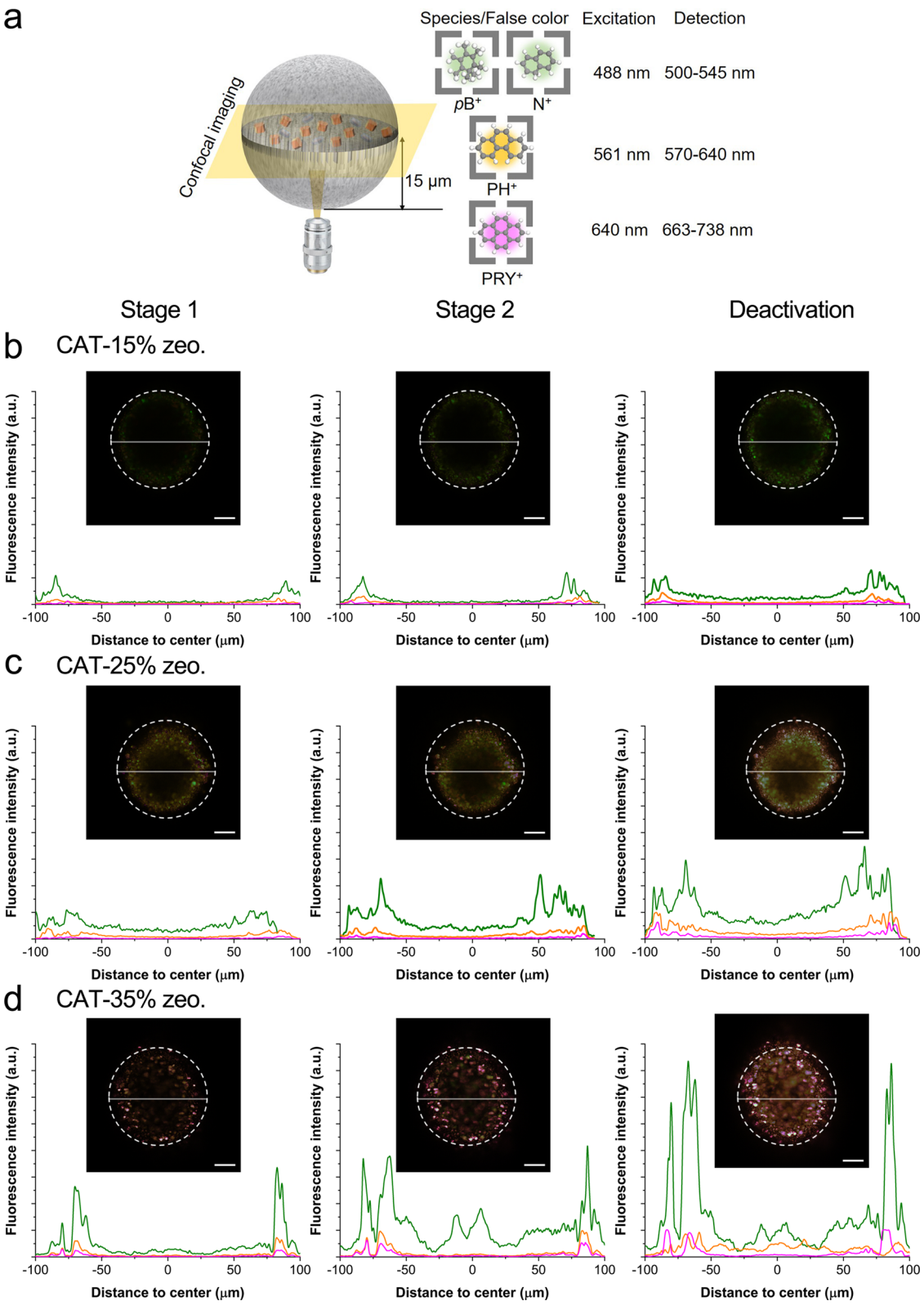

Figure 6. Spatiotemporal-resolved carbonaceous species within catalyst particles with different zeolite densities during MTH reactions. (a) Schematic spatial-resolved detection of carbonaceous species within catalyst particles by super-resolution CFM. The wavelengths of illumination and emission detection of CFM used in this work can cover the characteristic area of excitation and emission wavelengths of polymethylbenzenic (pB^+)/naphthalenic (N^+) (excitation: 488 nm and detection: 500−545 nm), phenanthrenic (PH^+) (excitation: 561 nm and detection: 570−640 nm), and pyrenic (PYR^+) carbocations (excitation: 640 nm and detection: 663−738 nm). Spatiotemporal evolutions of carbonaceous species within (b) CAT-15% zeo., (c) CAT-25% zeo., and (d) CAT-35% zeo. catalyst particles during the MTH reaction by super-resolution CFM. The CFM images show the fluorescence that originated from the overlap of three profiles with a laser excitation of 488 nm (detection at 500−545 nm, false color: green), 561 nm (detection at 570−640 nm, false color: orange), and 640 nm (detection at 663−738 nm, false color: pink). The images were taken in the plane 15 μm from the top. The fluorescence intensities along the selected solid line are also displayed.

https://doi.org/10.1021/jacs.3c14305
J. Am. Chem. Soc. 2024, 146, 4958−4972

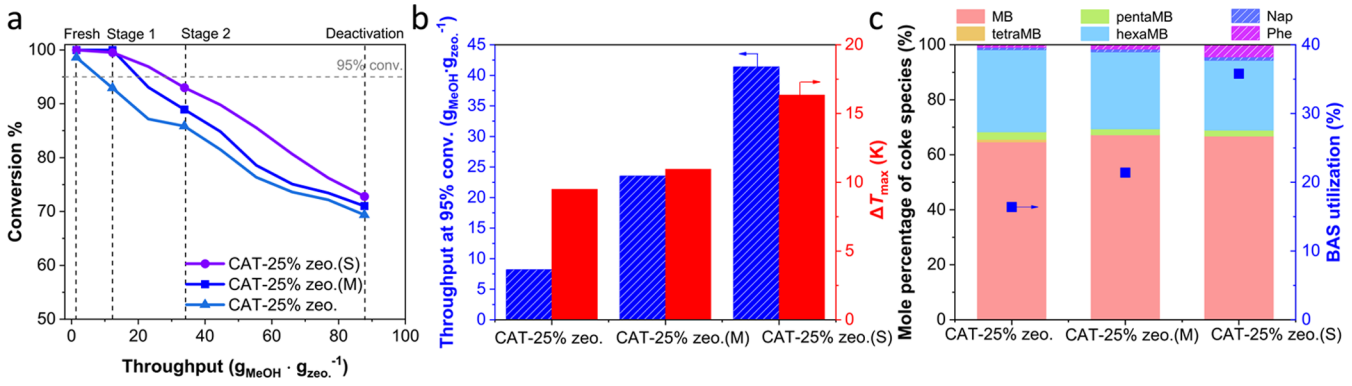

Figure 7. Effect of particle size on MTH reaction performance. (a) Methanol conversion as a function of methanol throughput over CAT.-25% zeo., CAT-25% zeo.(M), and CAT-25% zeo.(S) catalysts in a fixed-bed reactor. (b) Relation between methanol throughput (methanol conversion at 95% in (a), blue histogram)/maximum temperature rise (red histogram) and the particle size of the catalyst for MTH reactions. (c) Detailed components of coke species with molecular mass smaller than 200 Da (histogram) measured by solution-extraction experiments and BAS utilization (blue square) measured by diffuse reflectance infrared transform spectroscopy in deactivated catalysts. The initial reaction temperature is 623 K, and the weight hourly space velocity is 22.1 $g_{MeOH} \cdot g_{zeo.}^{-1} \cdot h^{-1}$ in a fixed-bed reactor.

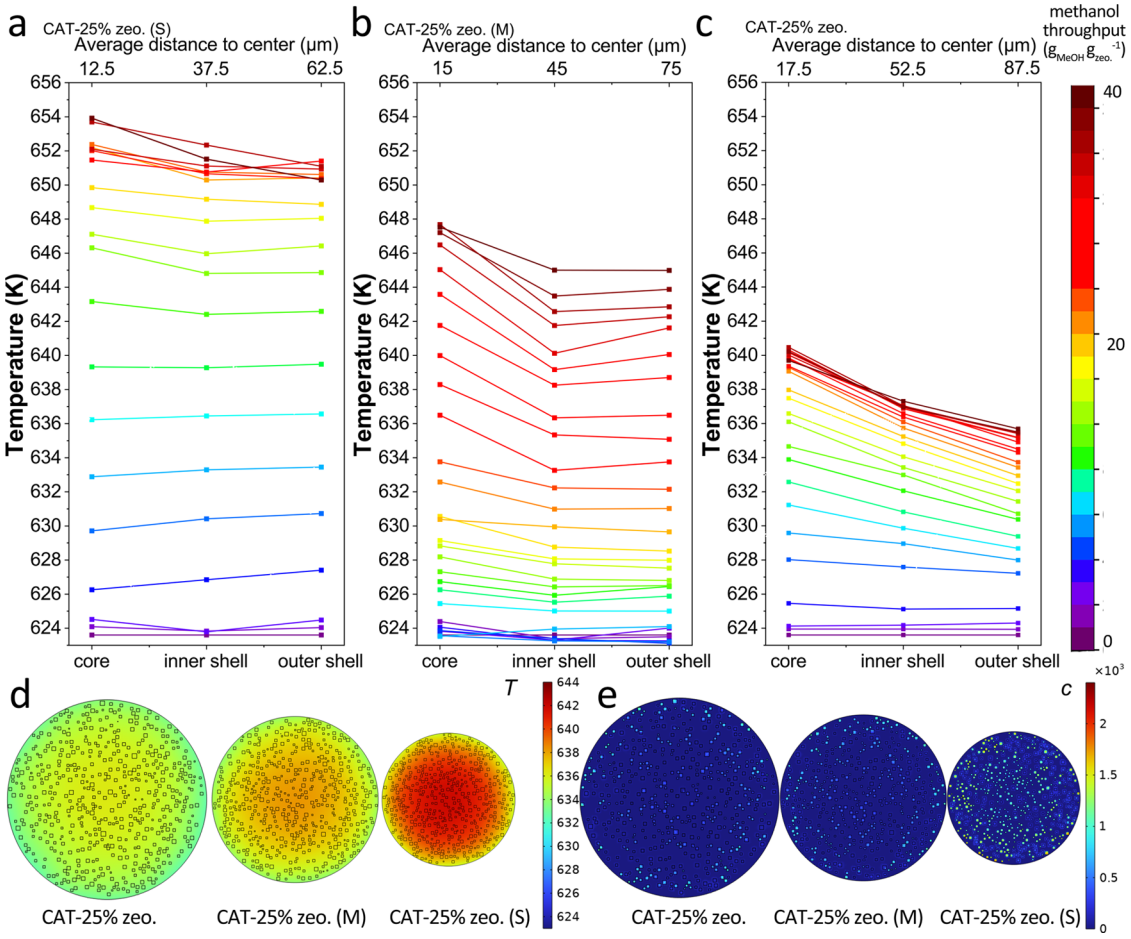

Figure 8. Effect of particle size on temperature heterogeneity within an individual catalyst. Spatiotemporal evolutions of temperature rise within individual (a) CAT-25% zeo., (b) CAT-25% zeo.(M), and (c) CAT-25% zeo.(S) catalyst particles by ratiometric thermometry using confocal UL microscopy during MTH reactions. The initial reaction temperature is 623 K, catalyst loading in the reaction cell is 2 mg, and weight hourly space velocity is 22.1 $g_{MeOH} \cdot g_{zeo.}^{-1} \cdot h^{-1}$. The inlet of nitrogen to carry the methanol saturated steam at room temperature is 1.5 $mL \cdot min^{-1}$. Simulation results of the spatial distribution of (d), maximum temperature rise (unit: K) during the MTH reaction and (e) PAHs (unit: $g \cdot m_{zeo.}^{-3}$) within the deactivated catalyst with particle sizes of 320 μm (CAT.-25% zeo.), 300 μm (CAT-25% zeo.(M)), and 270 μm (CAT-25% zeo. (S)) and 25% amounts of H-ZSM-5 zeolites. The square represents the zeolites. The initial simulation temperature is 623 K, and the weight hourly space velocity is 22.1 $g_{MeOH} \cdot g_{zeo.}^{-1} \cdot h^{-1}$.

higher temperature rise in the CAT-35% zeo. sample promotes the utilization of BAS with methanol to form sufficient amounts of HCP species. For the deactivated CAT-15% zeo., CAT-25% zeo. and CAT-35% zeo. particles, the relative

https://doi.org/10.1021/jacs.3c14305
J. Am. Chem. Soc. 2024, 146, 4958−4972

residual BAS values in the plane at z = 15 μm are, respectively, 0.54, 0.32, and 0.11 (see Supporting Note 6).

As shown in Figure 6a, implementing super-resolution CFM can visualize the spatiotemporal distribution of carbonaceous species in the plane at z = 15 μm within catalyst particles. As shown in Figure 6b, for the CAT-15% zeo. particle, the formation of polymethylbenzenic (pB^+) or naphthalenic (N^+) (excitation: 488 nm and detection: 500−545 nm, false color: green) mainly occurs at the edge of the particle through the initial stage to fully deactivation. This is further validated by the higher relative residual BAS at the internal region compared to that at the outer-shell region based on the IRM with the CAT-15% zeo. sample. The fluorescence intensities of phenanthrenic (PH^+) (excitation: 561 nm and detection: 570−640 nm, false color: orange) and pyrenic (PYR^+) carbocations (excitation: 640 nm and detection: 663−738 nm, false color: pink) for the CAT-15% zeo. particle are significantly weaker compared to those for CAT-25% zeo. and CAT-35% zeo. particles. As shown in Figure 4c, as MTH proceeds, the temperature at the core region is at most 2 K higher than that at the outer shell for the CAT-15% zeo. particle. Such a small heterogeneity in temperature within the CAT-15% zeo. particle cannot differentiate the thermal activation of HCP species at different regions of the particle. In addition, the temperature rise within CAT-15% zeo. cannot fully activate pB^+; thus, these pB^+ are the main inactivated species to block the pore and cover the BAS of zeolites. Therefore, the dominant eggshell-like distribution of carbonaceous species in the CAT-15% zeo. particle results from the enriched concentration of methanol at the particle edge, which is imposed by diffusion limitation, as evidenced by Figure S32. For the CAT-35% zeo. particle, in Figure 6d, compared to the fluorescence images of CAT-15% and CAT-25%, the fluorescence intensity of pB^+ or N^+ within particles is significantly higher, and the presence of the fluorescence signal of pB^+ or N^+ at the core and inner-shell regions can be observed. This indicates that the higher temperature rise within catalyst particles with higher active site density (Figure 4e) can effectively facilitate the formation of HCP species even though there is a relatively low methanol concentration at the internal region of particles. This can be verified by the lower relative residual BAS at the internal region of CAT-35% zeo. particles compared to that of CAT-15% zeo. or CAT-25 zeo. particles, as shown in Figure 5d. In addition, the uniform distribution of the fluorescence signal of PH^+ can be observed in deactivated CAT-35% zeo., which illustrates that the higher temperature rise within the catalyst can not only fully activate pB^+ but also permit the ring extending of pB^+ to polycyclic aromatic hydrocarbons (PAHs, e.g., PH^+). Based on the simulation results (Supporting Note 6), we can argue that the trends of coke distribution observed in the plane at z = 15 μm within CAT-15% zeo., CAT-25% zeo. and CAT-35% zeo. catalysts can be representative and reflect the trends of coke distribution at the middle plane of different catalysts. Such qualitative trends in coke distribution can, in principle, facilitate the understanding of the utilization of BAS at different regions of different catalysts. As a result, the higher temperature rise aroused by high zeolite density promotes the conversion of methanol with BAS and pB^+, which enlarges the throughput of methanol at the low start-up temperature.

Effect of Particle Size on Temperature Heterogeneity and Catalyst Efficiency. For the catalyst particle with the same BAS amount but different particle sizes, as shown in Figure 7b, decreasing the catalyst particle size can increase the maximum temperature rise and promote the methanol throughput at low start-up temperature. As shown in Figure 7c, for the deactivated CAT-25% zeo.(S) catalyst, the residual amounts of polyMBs and BAS are lower than those of the other two samples. This implies that a higher temperature increase in the catalyst with a small particle size leads to a more adequate transformation of polyMBs and utilization of BAS. At the initial stage of the MTH reaction, as shown in Figure 8a, the heating rate owing to the reaction exothermicity at the core region in the CAT-25% zeo.(S) catalyst is significantly faster than that in the other two catalysts, which can be explained as the rapid diffusion of methanol inward the catalyst center with a small particle size. Combined with simulation results in Figure S40, once the hotspot is formed at the core region, a lower temperature gradient attributed to the short distance between active sites is beneficial for reducing heat dissipation in a binder and facilitating heat conduction to neighboring active sites. Therefore, by using UL imaging, as shown in Figure 8a, it can be clearly observed that in the CAT-25% zeo.(S) sample, not only is the temperature rise elevated higher, but the temperature is also more homogeneously distributed within the catalyst. As shown in Figure S15, at z = 15 μm, the average diameters of the plane are 150, 170, and 190 μm for CAT-25% zeo.(S), CAT-25% zeo.(M), and CAT-25% zeo. particles, respectively. For the transfer of same heat from the core region to the outer shell of the particle at the xy-plane (e.g., z = 15 μm), prolonging distance results in a lower temperature at the outer shell and a lower average temperature over the cross section of interest. In addition, the corresponding temperature distribution at the middle plane within CAT.-25% zeo., CAT.-25% zeo.(S), and CAT.-25% zeo.(M) is extrapolated, as shown in Figure S13. Decreasing the particle size can effectively enhance the accessibility of BAS at the internal region of catalyst particles to the reactant.[11,67] As shown in Figure S14b, for CAT-25% zeo.(S) with small particle size, the fluorescence signal distribution of pB^+ or N^+ is relatively uniform throughout the particles at the initial stage of the MTH reaction. This implies that the intraparticle methanol concentration of CAT-25% zeo.(S) is higher than those of CAT-25% zeo.(M) and CAT-25% zeo. particles due to the shorter diffusion length. Combined with the temperature distribution within CAT-25% zeo.(S) shown in Figure 8a, a relatively higher and uniform distribution of methanol concentration and temperature jointly promote the transformation from HCP species to PAHs within the deactivated CAT-25% zeo.(S) sample. Correspondingly, as shown in Figure S14b, in the deactivated CAT-25% zeo.(S), the fluorescence signal of PH^+ and PRY^+ is strong and distributed uniformly in the internal region of CAT-25% zeo.(S). The sufficient transformation from pB^+ to PH^+ and PRY^+ can effectively improve the utilization of retained carbonaceous species and thus enhance methanol throughput.

Based on the observations at the individual particle level, we can profoundly illustrate the distinct temperature increase and different MTH reaction performances of catalysts with different active site densities and particle sizes. It is found that the higher BAS density can cause a higher temperature rise at the core region of the catalyst particle, and the smaller particle size can facilitate a relatively more uniform distribution of temperature inside the catalysts. This can have important indications for the practical manufacturing of industrial zeolite catalysts, in which the upper limit of content (i.e., mass fraction) of zeolites in individual catalysts is normally about

https://doi.org/10.1021/jacs.3c14305
J. Am. Chem. Soc. 2024, 146, 4958−4972

~60%.[12,52,68,69] We fabricated a zeolite catalyst with higher BAS density (i.e., the content of zeolite of 60%) and smaller particle size (named CAT-60% zeo.-130 μm), showing (as in Figure S29) that the temperature rise in sample CAT-60% zeo.-130 μm is significantly higher (~5 K in average) than that in sample CAT-35% zeo. during the MTH reaction. As expected, the methanol throughput (at a methanol conversion of 95%) on CAT-60% zeo.-130 μm (i.e., 45 $g_{MeOH}{\cdot}g_{zeo.}^{-1}$) is 2 times higher than that on CAT-35%-zeo. sample (i.e., 20 $g_{MeOH}{\cdot}g_{zeo.}^{-1}$) at a low start-up temperature of 623 K. This clearly illustrates that the temperature heterogeneity within individual catalyst particles can formulate the catalyst particle with higher methanol throughput.

CONCLUSIONS

In this study, we propose a confocal two-photon microscopy-based approach to measure the spatiotemporal variation of temperature within individual catalysts during catalytic reactions, utilizing the ratiometric thermometry of embedded $NaYF_4$@SiO_2 nanothermometers. In doing so, we first employ microfluidic chips for controllable fabrication of catalyst particles by incorporating zeolites and luminescence nanothermometers, with the aim of mimicking industrial catalysts. We then focus on the industrially important MTH reaction catalyzed by H-ZSM-5, a typical exothermic reaction, to investigate the temperature-dependent activation of HCP species at the individual catalyst level. Through the analysis of DFT calculation results, we determine that a higher temperature rise, particularly under low start-up temperatures, leads to the full activation of polyMBs. Furthermore, we employ a combination of multimodal imaging techniques (UL imaging, super-resolution CFM, and IRM) along with versatile simulations to profoundly elucidate the effect of temperature heterogeneity on local catalytic performance and vice versa. Our findings reveal that increasing the zeolite density, thereby decreasing the heat conductivity coefficient of the catalyst particles, reduces heat dissipation at the catalyst level. Therefore, increasing the BAS density results in a local temperature rise that excites the activation of polyMBs at specific positions and accelerates the release of reaction heat. Consequently, the overall temperature rise within individual catalyst particles increases with increasing zeolite density. Moreover, reducing the catalyst particle size decreases heat dissipation and temperature gradient during heat conduction between active sites, leading to a higher maximum temperature rise and more even temperature distribution throughout the particle. As a result, catalyst particles with higher BAS densities or smaller particle sizes exhibit improved utilization of BAS, activation of polyMBs in the aromatic-based cycle, and transformation of polyMBs to PAHs, ultimately enhancing the methanol throughput. As a showcase in the context of the MTH reaction, we emphasize the importance of considering temperature heterogeneity within individual catalyst particles as a crucial factor in the rational design of catalyst particles.

In conclusion, this study presents an approach to investigate the spatiotemporal heterogeneity of temperature and its impact on the efficiency of active sites as well as the activation and formation of guest molecules within individual catalyst particles. This is achieved through the implementation of functional nanosensors and multimodal imaging techniques. The proposed method offers a comprehensive perspective on the overall catalytic performance at the individual catalyst particle level, encompassing reaction kinetics, mass transport, and heat transfer. Future prospects involve the utilization of diverse types of nanosensors and confocal microscopies to obtain spatiotemporal-resolved panoramic insights into the catalytic process, including local temperature distribution, active site utilization, and intermediate species formation. Ultimately, this approach holds significant importance in advancing our understanding of reaction mechanisms and kinetics within single catalyst particles of industrial relevance.

METHODS

Fabrication and Characterization of Catalyst Particles. The microfluidic chips were employed for the fabrication of catalyst particles containing zeolites and nanofunctional sensors.[50] Adjusting the content of zeolites in the raw materials and the flow rate of the water phase in the microchannel can regulate the contents of zeolites in the catalyst and particle size of the catalyst, respectively. Synthetic details are introduced in Supporting Notes 5. The morphology and particle size of catalysts were observed with a Hitachi TM3000. The nitrogen isothermal adsorption−desorption was conducted using a Micromeritics ASAP 2020 to analyze the textural properties of catalysts. NH_3-temperature-programmed desorption profiles of catalysts were recorded on a Micrometric 2920 to obtain acid amounts of catalyst particles. The characterization methods for the composition, morphology, phase purity, textural property, and acidity of H-ZSM-5 zeolites and $NaYF_4$@SiO_2 are introduced in Supporting Notes 3. The heat conductivity coefficient of the SiO_2 matrix and H-ZSM-5 zeolites (samples were pressed into a ø13 × 3 mm^2 wafer) was measured by a thermal constant analyzer (Hot Disck TPS2500s).

Catalyst Performance Evaluation. The catalyst performance was evaluated in a fixed-bed reactor. The initial temperature of the catalyst bed was set to 623 K, the weight hourly space velocity (WHSV) of methanol was set to 22.1 $g_{MeOH}{\cdot}g_{zeo.}^{-1}{\cdot}h^{-1}$, and the partial pressure of methanol was 0.28 bar by flowing nitrogen. Online analysis of the gas products was performed with an Agilent 7890B gas chromatograph equipped with an flame ionization detection (FID) detector and a PoraPLOT Q-HT capillary column. The conversion and selectivity were calculated on a CH_2 basis.

Characterizations of Carbonaceous Species and BAS in Catalyst Particles. The coke species in the catalysts were analyzed by solution-extraction experiments. The relative changes in the Brönsted acid sites were detected by diffuse reflectance infrared spectroscopy. Experiment details are introduced in Supporting Notes 3.

Upconversion Luminescence Imaging by Confocal Two-Photon Microscopy. As shown in Figure S9, we employed a multiphoton confocal microscope (Nikon AX R MP) equipped with a high-working-distance 40×/0.80 objective lens (Nikon CFI Apo NIR 40X W), a two-photon light source (Spectra-Physics Mai Tai HP), and detector channels that can simultaneously record the intensity of two different wavelengths. The experiments of ratiometric thermometry employed in this work are introduced in the following. About 2 mg of catalyst samples were loaded in an in situ reaction cell, and then catalysts were purged with nitrogen at 623 K. To keep the same WHSV (22.1 $g_{MeOH}{\cdot}g_{zeo.}^{-1}{\cdot}h^{-1}$) of methanol in the cell as that in the fixed-bed reactor, the inlet of nitrogen was set to 2, 1.5, and 1 mL·min^{-1} for CAT.-35% zeo., CAT.-25% zeo. or CAT.-15% zeo. catalysts, respectively. The methanol saturated steam was carried by nitrogen at room temperature. In Figure 4a, the focal plane of the catalyst particle was selected to be a plane 15 μm from the top. At the focal plane, during MTH reactions, the spatiotemporal evolutions in the luminescence intensity of $NaYF_4$@SiO_2 at 510−570 nm (green channel) and 625−750 nm (red channel) were collected at 5 s intervals by two independent detectors with corresponding filters, respectively, excited by continuous-wave and pulsed 980 nm lasers (2 W excitation power). Using the same excitation power of lasers can avoid the interference of excitation power on red-to-green ratio measurements.[57] During the MTH reaction, the typical spatial-resolved luminescence intensities of $NaYF_4$@SiO_2 in catalysts collected at 510−570 nm (green channel) and 625−750 nm (red

https://doi.org/10.1021/jacs.3c14305
J. Am. Chem. Soc. 2024, 146, 4958−4972

channel) are shown in Figure S10. The local red-to-green ratio was calculated by the local luminescence intensity ratio I_2/I_1. Then, based on the calibration curve shown in Figure 2d, the local temperature within the catalyst particle can be calculated. In Figure 4b, we divided the spherical cross section of the catalyst into the core, inner-shell, and outer-shell regions to clearly represent the temperature gradient within the individual catalyst particle (Figure 4c−e). UL spectra of $NaYF_4$@SiO_2 in ensemble catalyst particles were obtained via a fluorescence spectrometer (Edinburgh FS5), in which a heating platform (Linkam HFS600E-PB2) was attached.

Super-Resolution Confocal Fluorescence Microscope. The spatial distribution of coke species within the deactivated catalyst particle is visualized by a super-resolution CFM. Based on our previous work[48] and theoretical calculation by time-dependent density functional theory,[70,71] in Figure 6a, the calculated excitation wavelengths of polymethylbenzenic (pB^+)/naphthalenic (N^+), phenanthrenic (PH^+), and pyrenic (PYR^+) carbocations were situated around 480, 560, and 640 nm, respectively, and the corresponding emission wavelengths were located in the ranges of 500−520, 620−630, and 670−700 nm, respectively. The sufficiently close wavelengths of illumination and emission detection of super-resolution CFM were used in this work, which can cover the characteristic areas of excitation and emission wavelengths of pB^+/N^+, PH^+, and PYR^+. In Figures 6b−d and S14, the super-resolution CFM images showed the fluorescence that originated from the overlap of three profiles with laser excitation of 488 nm (detection at 500−545 nm, false color: green), 561 nm (detection at 570−640 nm, false color: red), and 640 nm (detection at 663−738 nm, false color: orange). The images were taken in the plane at z = 15 μm from the top. The luminescence intensity ratios I_{561}/I_{488} and I_{640}/I_{488}, where intensities of I_{488}, I_{561}, and I_{640} are the integrated areas of the bands at, respectively, 500−545, 570−640 and 663−738 nm, were used to estimate the relative proportion of PAH species within the catalyst.

Infrared Microscopic Imaging. Before the IRM imaging, the spent catalysts were regenerated by air with a flow of 10 mL·min^{-1} at 823 K in an in situ reaction cell. The MTH reaction conditions for IRM imaging were similar to those for ratiometric thermometry in an in situ reaction cell. When a certain reaction stage was reached (Figure 3a), the inlet was switched from methanol/nitrogen to nitrogen, and IR spectra were collected along different positions of the catalyst, as shown in Figure 5a. As shown in Figure 5a, the IR spectra from the rim to the center of the catalyst particle were obtained by adjusting the catalyst position that can be opposite to the detection window through the electric displacement table. As shown in Figures S23 and S27, the deconvolution method was used to fit the IR band from 3200 to 3800 cm^{-1}. The positions of three Gaussian bands were 3740 cm^{-1} (isolated silanol), 3650 cm^{-1} (hydroxyls in BAS), and 3550 cm^{-1} (silanol nests), respectively.[72] In this work, the ratio of the integral area of the Gaussian band (position at 3650 cm^{-1}) between the spent and fresh samples was used to calculate the relative changes in BAS at the corresponding region within an individual particle. The maximum signal of BAS in the corresponding fresh catalyst particle was used as a baseline for normalization to show the relative changes in BAS, as shown in Figure 5b−d. To avoid the effect of water on the BAS measurements, the IR spectra were collected under the nitrogen atmosphere at 623 K. The detailed process was as follows: when a certain reaction stage was reached (Figure 3a), the inlet was switched from methanol/nitrogen to nitrogen, and IR spectra were collected along different positions of the catalyst, as shown in Figure 5a.

Simulations. The reaction kinetics−diffusion−heat transfer simulations were used to simulate the spatiotemporal evolutions of methanol, HCP species, polycyclic aromatic hydrocarbons, Brönsted acid sites, and temperature within individual catalyst particles with different active densities and particle sizes. The reaction−diffusion−heat transfer model was developed based on the reaction−diffusion model in our previous work.[48,73,74] As shown in Figure 8d, an example catalyst pellet formed with the randomly distributed H-ZSM-5 zeolites could be split into micropore zeolite (square) and mesopore regions (the binder was considered to be silica). A multi-region model and code were developed in previous work.[73] Each region was controlled by its own PDEs with coupling boundary conditions. The detailed description of PDEs and parameters of reaction kinetics, molecular diffusivity, and adsorption is introduced in Supporting Note 9 in the Supporting Information. Employing the detailed- or microkinetics of MTH reactions in reaction−diffusion−heat transfer is an appealing idea. However, constructing such a model not only requires a complicated reaction network and kinetics of MTH reactions but also involves the diffusion and adsorption of the reactant, intermedia, and products. Therefore, in this work, the lumped reaction kinetics was employed, which was validated by experiments in our previous work,[48,75] and the activation energy of the reaction was estimated from refs 59,62,76−78. The intracrystalline diffusivity D_i values of hydrocarbons and water were obtained from ref 79 and are listed in Table S6. The intracrystalline diffusivity of methanol and adsorption isotherms of hydrocarbons and methanol at 623 K were simulated by molecular dynamics and Monte Carlo simulations (detailed simulation methods are shown in Supporting Note 9 in the Supporting Information). The effects of H-ZSM-5 zeolite content and catalyst particle size on acid site utilization, carbonaceous species formation, and temperature variations were simulated.

■ ASSOCIATED CONTENT

Supporting Information

The Supporting Information is available free of charge at https://pubs.acs.org/doi/10.1021/jacs.3c14305.

Materials; characterization methods of materials; preparation and characterization of nanothermometry; preparation and characterization of catalyst particles; multimodal imaging techniques; methanol-to-hydrocarbons catalyzed by H-ZSM-5 zeolites at different temperatures; methanol-to-hydrocarbons catalyzed by catalyst particles and simulations; other supplementary results and discussions (PDF)

■ AUTHOR INFORMATION

Corresponding Authors

Mingbin Gao − *National Engineering Research Center of Lower-Carbon Catalysis Technology, Dalian National Laboratory for Clean Energy, Dalian Institute of Chemical Physics, Chinese Academy of Sciences, Dalian 116023, People's Republic of China;* orcid.org/0000-0002-7143-2658; Email: mbgao@dicp.ac.cn

Mao Ye − *National Engineering Research Center of Lower-Carbon Catalysis Technology, Dalian National Laboratory for Clean Energy, Dalian Institute of Chemical Physics, Chinese Academy of Sciences, Dalian 116023, People's Republic of China;* orcid.org/0000-0002-7078-2402; Email: maoye@dicp.ac.cn

Authors

Yu Tian − *National Engineering Research Center of Lower-Carbon Catalysis Technology, Dalian National Laboratory for Clean Energy, Dalian Institute of Chemical Physics, Chinese Academy of Sciences, Dalian 116023, People's Republic of China; University of Chinese Academy of Sciences, Beijing 10049, People's Republic of China*

Hua Xie − *National Engineering Research Center of Lower-Carbon Catalysis Technology, Dalian National Laboratory for Clean Energy, Dalian Institute of Chemical Physics, Chinese Academy of Sciences, Dalian 116023, People's Republic of China;* orcid.org/0000-0003-2091-6457

Shuliang Xu − *National Engineering Research Center of Lower-Carbon Catalysis Technology, Dalian National Laboratory for Clean Energy, Dalian Institute of Chemical*

https://doi.org/10.1021/jacs.3c14305
J. Am. Chem. Soc. 2024, 146, 4958−4972

Physics, Chinese Academy of Sciences, Dalian 116023, People's Republic of China

Zhongmin Liu − *National Engineering Research Center of Lower-Carbon Catalysis Technology, Dalian National Laboratory for Clean Energy, Dalian Institute of Chemical Physics, Chinese Academy of Sciences, Dalian 116023, People's Republic of China; University of Chinese Academy of Sciences, Beijing 10049, People's Republic of China;* orcid.org/0000-0002-7999-2940

Complete contact information is available at: https://pubs.acs.org/10.1021/jacs.3c14305

Author Contributions

[§]Y.T. and M.G. contributed equally.

Notes

The authors declare no competing financial interest.

■ ACKNOWLEDGMENTS

The authors thank the financial support from the National Natural Science Foundation of China, China (Grant Nos. 22293021, 22208337, 22288101, and 21991093) and the Strategic Priority Research Program of the Chinese Academy of Sciences, China (Grant No. XDA21030200). The authors also thank the kind help from Xuelian Zhou, Dr. Qinglong Qiao, and Prof. Zhaochao Xu in Dalian Institute of Chemical Physics, Chinese Academy of Sciences for fruitful investigation and discussion on two-photon imaging experiments, Dr. Hui Xu from the First Affiliated Hospital of Dalian Medical University for the help in two-photon imaging experiments, Dr. Peng Du from Ningbo University for the measurements of UL spectra, Zhenghao Jia in Dalian Institute of Chemical Physics, Chinese Academy of Sciences for the help in iDPC-STEM, Dr. Peifang Yan in Dalian Institute of Chemical Physics, Chinese Academy of Sciences for the intelligent gravimetric analyzer measurements, and Dr. Li Wang in Dalian Institute of Chemical Physics, Chinese Academy of Sciences for the fruitful discussion in MALDI FT-ICR mass spectra analysis. The authors thank the staff from BL06B1, BL20U and BL11B beamline of Shanghai Synchrotron Radiation Facility (SSRF) for assistance during IRM and X-ray absorption spectra data collection.

■ REFERENCES

(1) Dusselier, M.; Davis, M. E. Small-pore zeolites: synthesis and catalysis. *Chem. Rev.* **2018**, *118*, 5265−5329.

(2) Liu, L.; Corma, A. Confining isolated atoms and clusters in crystalline porous materials for catalysis. *Nat. Rev. Mater.* **2021**, *6*, 244−263.

(3) Li, Y.; Yu, J. Emerging applications of zeolites in catalysis, separation and host−guest assembly. *Nat. Rev. Mater.* **2021**, *6*, 1156−1174.

(4) Wang, W.; Zhou, W.; Tang, Y.; Cao, W.; Docherty, S. R.; Wu, F.; Cheng, K.; Zhang, Q.; Copéret, C.; Wang, Y. Selective Oxidation of Methane to Methanol over Au/H-MOR. *J. Am. Chem. Soc.* **2023**, *145*, 12928−12934.

(5) Vogt, C.; Weckhuysen, B. M. The concept of active site in heterogeneous catalysis. *Nat. Rev. Chem.* **2022**, *6*, 89−111.

(6) Gordon, C. P.; Engler, H.; Tragl, A. S.; Plodinec, M.; Lunkenbein, T.; Berkessel, A.; Teles, J. H.; Parvulescu, A.-N.; Copéret, C. Efficient epoxidation over dinuclear sites in titanium silicalite-1. *Nature* **2020**, *586*, 708−713.

(7) Hartman, T.; Geitenbeek, R. G.; Wondergem, C. S.; van der Stam, W.; Weckhuysen, B. M. Operando Nanoscale Sensors in Catalysis: All Eyes on Catalyst Particles. *ACS Nano* **2020**, *14*, 3725−3735.

(8) Hartman, T.; Geitenbeek, R. G.; Whiting, G. T.; Weckhuysen, B. M. Operando monitoring of temperature and active species at the single catalyst particle level. *Nat. Catal.* **2019**, *2*, 986−996.

(9) Yarulina, I.; Kapteijn, F.; Gascon, J. The importance of heat effects in the methanol to hydrocarbons reaction over ZSM-5: on the role of mesoporosity on catalyst performance. *Catal. Sci. Technol.* **2016**, *6*, 5320−5325.

(10) Moosavi, S. M.; Novotny, B. Á.; Ongari, D.; Moubarak, E.; Asgari, M.; Kadioglu, Ö.; Charalambous, C.; Ortega-Guerrero, A.; Farmahini, A. H.; Sarkisov, L.; Garcia, S.; Noé, F.; Smit, B. A data-science approach to predict the heat capacity of nanoporous materials. *Nat. Mater.* **2022**, *21*, 1419−1425.

(11) Whiting, G. T.; Nikolopoulos, N.; Nikolopoulos, I.; Chowdhury, A. D.; Weckhuysen, B. M. Visualizing pore architecture and molecular transport boundaries in catalyst bodies with fluorescent nanoprobes. *Nat. Chem.* **2019**, *11*, 23−31.

(12) Mitchell, S.; Michels, N.-L.; Kunze, K.; Pérez-Ramírez, J. Visualization of hierarchically structured zeolite bodies from macro to nano length scales. *Nat. Chem.* **2012**, *4*, 825−831.

(13) Buurmans, I. L. C.; Ruiz-Martínez, J.; Knowles, W. V.; van der Beek, D.; Bergwerff, J. A.; Vogt, E. T. C.; Weckhuysen, B. M. Catalytic activity in individual cracking catalyst particles imaged throughout different life stages by selective staining. *Nat. Chem.* **2011**, *3*, 862−867.

(14) Heenan, T. M. M.; Mombrini, I.; Llewellyn, A.; Checchia, S.; Tan, C.; Johnson, M. J.; Jnawali, A.; Garbarino, G.; Jervis, R.; Brett, D. J. L.; Di Michiel, M.; Shearing, P. R. Mapping internal temperatures during high-rate battery applications. *Nature* **2023**, *617*, 507−512.

(15) Gao, M.; Ye, M.; Liu, Z. Emerging techniques to monitor temperature and supply heat for multiscale solid-based catalysis processes. *Curr. Opin. Chem. Eng.* **2023**, *42*, No. 100969.

(16) Aitbekova, A.; Zhou, C.; Stone, M. L.; Lezama-Pacheco, J. S.; Yang, A.-C.; Hoffman, A. S.; Goodman, E. D.; Huber, P.; Stebbins, J. F.; Bustillo, K. C.; Ercius, P.; Ciston, J.; Bare, S. R.; Plessow, P. N.; Cargnello, M. Templated encapsulation of platinum-based catalysts promotes high-temperature stability to 1,100 °C. *Nat. Mater.* **2022**, *21*, 1290−1297.

(17) Cnudde, P.; Demuynck, R.; Vandenbrande, S.; Waroquier, M.; Sastre, G.; Speybroeck, V. V. Light Olefin Diffusion during the MTO Process on H-SAPO-34: A Complex Interplay of Molecular Factors. *J. Am. Chem. Soc.* **2020**, *142*, 6007−6017.

(18) Zimmerman, P. M.; Tranca, D. C.; Gomes, J.; Lambrecht, D. S.; Head-Gordon, M.; Bell, A. T. Ab Initio Simulations Reveal that Reaction Dynamics Strongly Affect Product Selectivity for the Cracking of Alkanes over H-MFI. *J. Am. Chem. Soc.* **2012**, *134*, 19468−19476.

(19) Borodina, E.; Meirer, F.; Lezcano-González, I.; Mokhtar, M.; Asiri, A. M.; Al-Thabaiti, S. A.; Basahel, S. N.; Ruiz-Martinez, J.; Weckhuysen, B. M. Influence of the Reaction Temperature on the Nature of the Active and Deactivating Species during Methanol to Olefins Conversion over H-SSZ-13. *ACS Catal.* **2015**, *5*, 992−1003.

(20) Borodina, E.; Sharbini Harun Kamaluddin, H.; Meirer, F.; Mokhtar, M.; Asiri, A. M.; Al-Thabaiti, S. A.; Basahel, S. N.; Ruiz-Martinez, J.; Weckhuysen, B. M. Influence of the Reaction Temperature on the Nature of the Active and Deactivating Species During Methanol-to-Olefins Conversion over H-SAPO-34. *ACS Catal.* **2017**, *7*, 5268−5281.

(21) Yuan, J.; Liu, Z.; Wu, Y.; Han, J.; Tang, X.; Li, C.; Chen, W.; Yi, X.; Zhou, J.; Krishna, R.; Sastre, G.; Zheng, A. Thermal resistance effect on anomalous diffusion of molecules under confinement. *Proc. Natl. Acad. Sci. U.S.A.* **2021**, *118*, No. e2102097118.

(22) Terlingen, B. J. P.; Arens, T.; van Swieten, T. P.; Rabouw, F. T.; Prins, T.; de Beer, M. M.; Meijerink, A.; Ahr, M.; Hutter, E. M.; van Lare, C.; Weckhuysen, B. M. Bifunctional Europium for Operando Catalyst Thermometry in an Exothermic Chemical Reaction. *Angew. Chem., Int. Ed.* **2022**, *61*, No. e202211991.

(23) Buurmans, I. L. C.; Weckhuysen, B. M. Heterogeneities of individual catalyst particles in space and time as monitored by spectroscopy. *Nat. Chem.* **2012**, *4*, 873−886.
(24) Qian, Q.; Ruiz-Martínez, J.; Mokhtar, M.; Asiri, A. M.; Al-Thabaiti, S. A.; Basahel, S. N.; van der Bij, H. E.; Kornatowski, J.; Weckhuysen, B. M. Single-Particle Spectroscopy on Large SAPO-34 Crystals at Work: Methanol-to-Olefin versus Ethanol-to-Olefin Processes. *Chem. - Eur. J.* **2013**, *19*, 11204−11215.
(25) Kärger, J.; Binder, T.; Chmelik, C.; Hibbe, F.; Krautscheid, H.; Krishna, R.; Weitkamp, J. Microimaging of transient guest profiles to monitor mass transfer in nanoporous materials. *Nat. Mater.* **2014**, *13*, 333−343.
(26) Remi, J. C. S.; Lauerer, A.; Chmelik, C.; Vandendael, I.; Terryn, H.; Baron, G. V.; Denayer, J. F. M.; Karger, J. The role of crystal diversity in understanding mass transfer in nanoporous materials. *Nat. Mater.* **2016**, *15*, 401−406.
(27) Simeone, M.; Salemme, L.; Allouis, C.; Volpicelli, G. Temperature profile in a reverse flow reactor for catalytic partial oxidation of methane by fast IR imaging. *AIChE J.* **2008**, *54*, 2689−2698.
(28) Koptyug, I. V.; Khomichev, A. V.; Lysova, A. A.; Sagdeev, R. Z. Spatially Resolved NMR Thermometry of an Operating Fixed-Bed Catalytic Reactor. *J. Am. Chem. Soc.* **2008**, *130*, 10452−10453.
(29) Smith, J. D.; Cappa, C. D.; Drisdell, W. S.; Cohen, R. C.; Saykally, R. J. Raman Thermometry Measurements of Free Evaporation from Liquid Water Droplets. *J. Am. Chem. Soc.* **2006**, *128*, 12892−12898.
(30) Jaque, D.; Vetrone, F. Luminescence nanothermometry. *Nanoscale* **2012**, *4*, 4301−4326.
(31) Geitenbeek, R. G.; Prins, P. T.; Albrecht, W.; van Blaaderen, A.; Weckhuysen, B. M.; Meijerink, A. NaYF4:Er3+,Yb3+/SiO2 Core/Shell Upconverting Nanocrystals for Luminescence Thermometry up to 900 K. *J. Phys. Chem. C* **2017**, *121*, 3503−3510.
(32) Zhou, J.; del Rosal, B.; Jaque, D.; Uchiyama, S.; Jin, D. Advances and challenges for fluorescence nanothermometry. *Nat. Methods* **2020**, *17*, 967−980.
(33) Bednarkiewicz, A.; Marciniak, L.; Carlos, L. D.; Jaque, D. Standardizing luminescence nanothermometry for biomedical applications. *Nanoscale* **2020**, *12*, 14405−14421.
(34) Arppe, R.; Hyppänen, I.; Perälä, N.; Peltomaa, R.; Kaiser, M.; Würth, C.; Christ, S.; Resch-Genger, U.; Schäferling, M.; Soukka, T. Quenching of the upconversion luminescence of NaYF4:Yb3+,Er3+ and NaYF4:Yb3+,Tm3+ nanophosphors by water: the role of the sensitizer Yb3+ in non-radiative relaxation. *Nanoscale* **2015**, *7*, 11746−11757.
(35) Jacobs, T. S.; van Swieten, T. P.; Vonk, S. J. W.; Bosman, I. P.; Melcherts, A. E. M.; Janssen, B. C.; Janssens, J. C. L.; Monai, M.; Meijerink, A.; Rabouw, F. T.; van der Stam, W.; Weckhuysen, B. M. Mapping Temperature Heterogeneities during Catalytic CO2Methanation with Operando Luminescence Thermometry. *ACS Nano* **2023**, *17*, 20053−20061.
(36) Wang, F.; Deng, R.; Liu, X. Preparation of core-shell NaGdF4 nanoparticles doped with luminescent lanthanide ions to be used as upconversion-based probes. *Nat. Protoc.* **2014**, *9*, 1634−1644.
(37) Geitenbeek, R. G.; Nieuwelink, A.-E.; Jacobs, T. S.; Salzmann, B. B. V.; Goetze, J.; Meijerink, A.; Weckhuysen, B. M. In Situ Luminescence Thermometry To Locally Measure Temperature Gradients during Catalytic Reactions. *ACS Catal.* **2018**, *8*, 2397−2401.
(38) Yarulina, I.; Chowdhury, A. D.; Meirer, F.; Weckhuysen, B. M.; Gascon, J. Recent trends and fundamental insights in the methanol-to-hydrocarbons process. *Nat. Catal.* **2018**, *1*, 398−411.
(39) Cesarini, A.; Mitchell, S.; Zichittella, G.; Agrachev, M.; Schmid, S. P.; Jeschke, G.; Pan, Z.; Bodi, A.; Hemberger, P.; Pérez-Ramírez, J. Elucidation of radical- and oxygenate-driven paths in zeolite-catalysed conversion of methanol and methyl chloride to hydrocarbons. *Nat. Catal.* **2022**, *5*, 605−614.
(40) Olsbye, U.; Svelle, S.; Bjørgen, M.; Beato, P.; Janssens, T. V. W.; Joensen, F.; Bordiga, S.; Lillerud, K. P. Conversion of Methanol to Hydrocarbons: How Zeolite Cavity and Pore Size Controls Product Selectivity. *Angew. Chem., Int. Ed.* **2012**, *51*, 5810−5831.
(41) DeLuca, M.; Janes, C.; Hibbitts, D. Contrasting Arene, Alkene, Diene, and Formaldehyde Hydrogenation in H-ZSM-5, H-SSZ-13, and H-SAPO-34 Frameworks during MTO. *ACS Catal.* **2020**, *10*, 4593−4607.
(42) Hwang, A.; Bhan, A. Deactivation of Zeolites and Zeotypes in Methanol-to-Hydrocarbons Catalysis: Mechanisms and Circumvention. *Acc. Chem. Res.* **2019**, *52*, 2647−2656.
(43) Ferri, P.; Li, C.; Paris, C.; Vidal-Moya, A.; Moliner, M.; Boronat, M.; Corma, A. Chemical and Structural Parameter Connecting Cavity Architecture, Confined Hydrocarbon Pool Species, and MTO Product Selectivity in Small-Pore Cage-Based Zeolites. *ACS Catal.* **2019**, *9*, 11542−11551.
(44) Kang, J. H.; Alshafei, F. H.; Zones, S. I.; Davis, M. E. Cage-Defining Ring: A Molecular Sieve Structural Indicator for Light Olefin Product Distribution from the Methanol-to-Olefins Reaction. *ACS Catal.* **2019**, *9*, 6012−6019.
(45) Li, C.; Paris, C.; Martínez-Triguero, J.; Boronat, M.; Moliner, M.; Corma, A. Synthesis of reaction-adapted zeolites as methanol-to-olefins catalysts with mimics of reaction intermediates as organic structure-directing agents. *Nat. Catal.* **2018**, *1*, 547−554.
(46) Lezcano-Gonzalez, I.; Campbell, E.; Hoffman, A. E. J.; Bocus, M.; Sazanovich, I. V.; Towrie, M.; Agote-Aran, M.; Gibson, E. K.; Greenaway, A.; De Wispelaere, K.; Van Speybroeck, V.; Beale, A. M. Insight into the effects of confined hydrocarbon species on the lifetime of methanol conversion catalysts. *Nat. Mater.* **2020**, *19*, 1081−1087.
(47) Omori, N.; Candeo, A.; Mosca, S.; Lezcano-Gonzalez, I.; Robinson, I. K.; Li, L.; Greenaway, A. G.; Collier, P.; Beale, A. M. Multimodal Imaging of Autofluorescent Sites Reveals Varied Chemical Speciation in SSZ-13 Crystals. *Angew. Chem., Int. Ed.* **2021**, *60*, 5125−5131.
(48) Gao, M.; Li, H.; Liu, W.; Xu, Z.; Peng, S.; Yang, M.; Ye, M.; Liu, Z. Imaging spatiotemporal evolution of molecules and active sites in zeolite catalyst during methanol-to-olefins reaction. *Nat. Commun.* **2020**, *11*, No. 3652.
(49) Chmelik, C.; Liebau, M.; Al-Naji, M.; Möllmer, J.; Enke, D.; Gläser, R.; Kärger, J. One-Shot Measurement of Effectiveness Factors of Chemical Conversion in Porous Catalysts. *ChemCatChem* **2018**, *10*, 5602−5609.
(50) Xu, S.; Nie, Z.; Seo, M.; Lewis, P.; Kumacheva, E.; Stone, H. A.; Garstecki, P.; Weibel, D. B.; Gitlin, I.; Whitesides, G. M. Generation of Monodisperse Particles by Using Microfluidics: Control over Size, Shape, and Composition. *Angew. Chem., Int. Ed.* **2005**, *44*, 724−728.
(51) Nieuwelink, A.-E.; Vollenbroek, J. C.; Tiggelaar, R. M.; Bomer, J. G.; van den Berg, A.; Odijk, M.; Weckhuysen, B. M. High-throughput activity screening and sorting of single catalyst particles with a droplet microreactor using dielectrophoresis. *Nat. Catal.* **2021**, *4*, 1070−1079.
(52) Tian, P.; Wei, Y.; Ye, M.; Liu, Z. Methanol to Olefins (MTO): From Fundamentals to Commercialization. *ACS Catal.* **2015**, *5*, 1922−1938.
(53) Zhang, Y.-J.; Ze, H.; Fang, P.-P.; Huang, Y.-F.; Kudelski, A.; Fernández-Vidal, J.; Hardwick, L. J.; Lipkowski, J.; Tian, Z.-Q.; Li, J.-F. Shell-isolated nanoparticle-enhanced Raman spectroscopy. *Nat. Rev. Methods Primers* **2023**, *3*, No. 36.
(54) Chen, J.; Gao, Y.; Wang, C.; Yin, Y.; Song, J.; Zeng, X.; Liu, Z.; Jiang, H. Effective regulation of upconversion luminescence in NaErF4 and NaErF4@SiO2 core-shell particles. *Ceram. Int.* **2022**, *48*, 14315−14322.
(55) Fu, D.; Maris, J. J. E.; Stanciakova, K.; Nikolopoulos, N.; van der Heijden, O.; Mandemaker, L. D. B.; Siemons, M. E.; Salas Pastene, D.; Kapitein, L. C.; Rabouw, F. T.; Meirer, F.; Weckhuysen, B. M. Unravelling Channel Structure−Diffusivity Relationships in Zeolite ZSM-5 at the Single-Molecule Level. *Angew. Chem., Int. Ed.* **2022**, *61*, No. e202114388.

https://doi.org/10.1021/jacs.3c14305
J. Am. Chem. Soc. 2024, 146, 4958−4972

(56) Foley, B. L.; Johnson, B. A.; Bhan, A. A Method for Assessing Catalyst Deactivation: A Case Study on Methanol-to-Hydrocarbons Conversion. *ACS Catal.* **2019**, *9*, 7065−7072.
(57) Würth, C.; Kaiser, M.; Wilhelm, S.; Grauel, B.; Hirsch, T.; Resch-Genger, U. Excitation power dependent population pathways and absolute quantum yields of upconversion nanoparticles in different solvents. *Nanoscale* **2017**, *9*, 4283−4294.
(58) Lide, D. R. *CRC Handbook of Chemistry and Physics*; CRC Press, 2005.
(59) De Wispelaere, K.; Hemelsoet, K.; Waroquier, M.; Van Speybroeck, V. Complete low-barrier side-chain route for olefin formation during methanol conversion in H-SAPO-34. *J. Catal.* **2013**, *305*, 76−80.
(60) DeLuca, M.; Kravchenko, P.; Hoffman, A.; Hibbitts, D. Mechanism and Kinetics of Methylating C6−C12 Methylbenzenes with Methanol and Dimethyl Ether in H-MFI Zeolites. *ACS Catal.* **2019**, *9*, 6444−6460.
(61) Khare, R.; Bhan, A. Mechanistic studies of methanol-to-hydrocarbons conversion on diffusion-free MFI samples. *J. Catal.* **2015**, *329*, 218−228.
(62) Montalvo-Castro, H.; DeLuca, M.; Kilburn, L.; Hibbitts, D. Mechanisms and Kinetics of the Dehydrogenation of C6−C8 Cycloalkanes, Cycloalkenes, and Cyclodienes to Aromatics in H-MFI Zeolite Framework. *ACS Catal.* **2023**, *13*, 99−112.
(63) Hoffman, A.; DeLuca, M.; Hibbitts, D. Restructuring of MFI Framework Zeolite Models and Their Associated Artifacts in Density Functional Theory Calculations. *J. Phys. Chem. C* **2019**, *123*, 6572−6585.
(64) Wei, Y.; Yuan, C.; Li, J.; Xu, S.; Zhou, Y.; Chen, J.; Wang, Q.; Xu, L.; Qi, Y.; Zhang, Q.; Liu, Z. Coke Formation and Carbon Atom Economy of Methanol-to-Olefins Reaction. *ChemSusChem* **2012**, *5*, 906−912.
(65) Svelle, S.; Joensen, F.; Nerlov, J.; Olsbye, U.; Lillerud, K.-P.; Kolboe, S.; Bjørgen, M. Conversion of Methanol into Hydrocarbons over Zeolite H-ZSM-5: Ethene Formation Is Mechanistically Separated from the Formation of Higher Alkenes. *J. Am. Chem. Soc.* **2006**, *128*, 14770−14771.
(66) Bjorgen, M.; Svelle, S.; Joensen, F.; Nerlov, J.; Kolboe, S.; Bonino, F.; Palumbo, L.; Bordiga, S.; Olsbye, U. Conversion of methanol to hydrocarbons over zeolite H-ZSM-5: On the origin of the olefinic species. *J. Catal.* **2007**, *249*, 195−207.
(67) Noh, G.; Zones, S. I.; Iglesia, E. Consequences of Acid Strength and Diffusional Constraints for Alkane Isomerization and β-Scission Turnover Rates and Selectivities on Bifunctional Metal-Acid Catalysts. *J. Phys. Chem. C* **2018**, *122*, 25475−25497.
(68) Weckhuysen, B. M. Chemical Imaging of Spatial Heterogeneities in Catalytic Solids at Different Length and Time Scales. *Angew. Chem., Int. Ed.* **2009**, *48*, 4910−4943.
(69) Whiting, G. T.; Chung, S.-H.; Stosic, D.; Chowdhury, A. D.; van der Wal, L. I.; Fu, D.; Zecevic, J.; Travert, A.; Houben, K.; Baldus, M.; Weckhuysen, B. M. Multiscale Mechanistic Insights of Shaped Catalyst Body Formulations and Their Impact on Catalytic Properties. *ACS Catal.* **2019**, *9*, 4792−4803.
(70) Hemelsoet, K.; Qian, Q.; De Meyer, T.; De Wispelaere, K.; De Sterck, B.; Weckhuysen, B. M.; Waroquier, M.; Van Speybroeck, V. Identification of Intermediates in Zeolite-Catalyzed Reactions by In Situ UV/Vis Microspectroscopy and a Complementary Set of Molecular Simulations. *Chem. - Eur. J.* **2013**, *19*, 16595−16606.
(71) Qian, Q.; Vogt, C.; Mokhtar, M.; Asiri, A. M.; Al-Thabaiti, S. A.; Basahel, S. N.; Ruiz-Martínez, J.; Weckhuysen, B. M. Combined Operando UV/Vis/IR Spectroscopy Reveals the Role of Methoxy and Aromatic Species during the Methanol-to-Olefins Reaction over H-SAPO-34. *ChemCatChem* **2014**, *6*, 3396−3408.
(72) Medeiros-Costa, I. C.; Dib, E.; Nesterenko, N.; Dath, J.-P.; Gilson, J.-P.; Mintova, S. Silanol defect engineering and healing in zeolites: opportunities to fine-tune their properties and performances. *Chem. Soc. Rev.* **2021**, *50*, 11156−11179.
(73) Li, H.; Ye, M.; Liu, Z. A multi-region model for reaction−diffusion process within a porous catalyst pellet. *Chem. Eng. Sci.* **2016**, *147*, 1−12.
(74) Gao, M.; Li, H.; Yang, M.; Zhou, J.; Yuan, X.; Tian, P.; Ye, M.; Liu, Z. A modeling study on reaction and diffusion in MTO process over SAPO-34 zeolites. *Chem. Eng. J.* **2019**, *377*, No. 119668.
(75) Yuan, X.; Li, H.; Ye, M.; Liu, Z. Kinetic modeling of methanol to olefins process over SAPO-34 catalyst based on the dual-cycle reaction mechanism. *AIChE J.* **2019**, *65*, 662−674.
(76) Van Speybroeck, V.; Van der Mynsbrugge, J.; Vandichel, M.; Hemelsoet, K.; Lesthaeghe, D.; Ghysels, A.; Marin, G. B.; Waroquier, M. First Principle Kinetic Studies of Zeolite-Catalyzed Methylation Reactions. *J. Am. Chem. Soc.* **2011**, *133*, 888−899.
(77) Joshi, Y. V.; Thomson, K. T. Brønsted Acid Catalyzed Cyclization of C7 and C8 Dienes in HZSM-5: A Hybrid QM/MM Study and Comparison with C6 Diene Cyclization. *J. Phys. Chem. C* **2008**, *112*, 12825−12833.
(78) Wang, S.; Chen, Y.; Wei, Z.; Qin, Z.; Liang, T.; Dong, M.; Li, J.; Fan, W.; Wang, J. Evolution of aromatic species in supercages and its effect on the conversion of methanol to olefins over H-MCM-22 zeolite: a density functional theory study. *J. Phys. Chem. C* **2016**, *120*, 27964−27979.
(79) Kärger, J.; Ruthven, D. M.; Theodorou, D. N. *Diffusion in Nanoporous Materials*; Wiley-VCH Verlag & Co. KGaA, 2012.

https://doi.org/10.1021/jacs.3c14305
J. Am. Chem. Soc. 2024, 146, 4958−4972